Development of a Controlled Environment Apparatus for Laser Micromachining Experiments

Department of Chemical Engineering

McGill University, Montréal

October 2018

A thesis submitted to McGill University in partial fulfillment of the requirements of the degree of Masters of Engineering

Contents

1 Introduction **1**

2 A Review of the Literature **3**

2.1 Surface Texturing of Metals 3

2.1.1 Accumulated Fluence 5

2.1.2 Structures & Wetting Properties 5

2.2 Surface Chemistry and Wetting Transition on Laser Textured Metals 7

2.3 Controlled Environment Apparatus 9

2.3.1 Interaction of fs Laser Beams with Glass 10

2.3.2 Gas, Plasma and Particle Environment 11

2.3.3 Substrate Interaction with Environment 13

3 Objectives **16**

4 Chamber Design & SOP Development **18**

4.1 Designs for a Controlled Environment Chamber 18

4.1.1 Design Considerations 19

4.1.2 Design Options 21

4.2 Prototype Chamber & SOP Design 26

4.2.1 Prototype Chamber 26

4.2.2 Proof of Concept Experiments 27

4.2.3 Design & SOP Contributions 31
4.3 Prototype Chamber Testing in Typical Experimental Conditions 32
4.3.1 Prototype Chamber for Gas & Vacuum Environment Experiments 33
4.3.2 Impact of Varying Laser & Scanning Parameters 38
4.4 Chamber Design Choice & Finalized SOP 44
4.4.1 Re-evaluation of Design Options 46
4.4.2 Design Considerations for the Cube 50

5 Nanoparticle Collection **54**
5.1 Proof of Concept Tests 54
5.1.1 Test Run 56
5.1.2 Configuration 1 58
5.1.3 Configuration 2 60
5.1.4 Impact 62
5.2 Experiments 62
5.2.1 Electric Field 63
5.2.2 Electric Charge 66
5.2.3 Discussion 70

6 Conclusion **73**
6.1 Conclusions from Chamber Design and SOP Development 73
6.2 Conclusions from the Nanoparticle Collection 74

7 Original Contributions **75**

8 Further Work **76**

Bibliography **78**

Appendices **84**

A Standard Operating Procedures **85**

A.1 Prototype Chamber 85

A.1.1 Finding the home position of the stage with the chamber 85

A.1.2 Sample Preparation & Loading 85

A.1.3 Connecting to Gas & Vacuum Lines 86

A.2 Cube Chamber 87

A.2.1 Sample Preparation & Loading 87

A.2.2 Connecting to Gas and Vacuum Lines 88

A.3 Analysis 88

A.3.1 Transfer into VTM in glove box 88

A.3.2 Notes on the VTM & XPS Apparatus 89

B Major Equipment Data **91**

B.1 Vacuum Pump 91

B.2 VTM 92

List of Figures

2.1 The gaussian profile of the laser beam at each spot is shown to overlap, resulting in the surface experiencing an accumulated fluence over the line. . . . 6

2.2 (a)The typical view of a water droplet on a flat surface where θ is the contact angle measured , (b)A Wenzel wetting state where a hydrophilic surface becomes superhydrophilic upon *roughening*, (c)The Cassie wetting state where air is trapped between the water droplet and the *roughened* surface. 7

2.3 Passing a laser beam through the glass results in an increase in beam diameter. In this image, the focusing lens has a focal length of 100 mm. 12

2.4 The interaction of a laser beam with the gas environment, the expanding plasma and the particle cloud. Adapted from Lehr et. al. (2014) 13

4.1 An illustration showing the laser beam path (in red) from the fs laser system to the 3-D axis stage. 19

4.2 CAD illustration of the 4-way Cross Chamber 22

4.3 CAD illustration of the 5-way Cross Chamber 23

4.4 CAD illustration of the Cubic Reactor 24

4.5 An image of the VTM showing the one-way valve for vacuum and glass window 24

4.6 An image of the prototype chamber fastened to the 3-D axis stage and connected to the gas and vacuum lines during an experiment. 27

4.7 Summary of the contributions to chamber design and SOP from the proof-of-concept experiments. 33
4.8 SEM images illustrating the surface topography of samples machined in He, N_2 and vacuum environment. All length scales are 10 μm. 36
4.9 Atomic composition of the samples prepared in the prototype chamber and transferred through a glove box to the VTM for surface chemsitry analysis in the XPS apparatus 37
4.10 Summary of the contributions to the design and SOP development from the chamber testing for gas and vacuum environments 39
4.11 SEM images illustrating A-Bumps; B-Undulating grooves; C-Ripply Bumps and D-Cones machined in N_2 (top row) and vacuum (bottom row) environment using settings for *aggregate* and *chaotic structures*. All length scales correspond to 5 μm. 42
4.12 Atomic composition of the samples micromachined with *aggregate* and *chaotic* structures in nitrogen and vacuum environments 43
4.13 The chamber design and SOP development flow chart was updated to reflect the findings of the topography experiments 45
4.14 A CAD image of the 5-way cross affixed to the 3D stage with posts at each corner to secure the chamber. 47
4.15 A CAD image of the cube affixed to the 3D stage with a 3D printed holder (left). The CAD of the holder is on the right. 48
4.16 A diagram of the electronic sample holder consisting of a servo motor in the cube chamber. 52
4.17 A diagram of the simple sample holder in the cube chamber. The 3D stage will be used to move the sample into the beam path. 53

5.1 The experiments conducted are summarised in the flow chart. In the yellow box are the proof-of-concept experiments which informed the plan of actual experiments in green. 55
5.2 Trial 1: SEM images of the copper collector (left, red) and the three patches machined consecutively on titanium (right, blue) at -100V. Scales correspond to 100 μm. 57
5.3 Trial 2: SEM images of the copper collector (left, red) and the three patches machined consecutively on titanium (right, blue) at +100V. Scale is 200 μm (left) and 500 μm (right). 57
5.4 Trial 3: SEM images of the copper collector (left, red) at +100 V and three patches consecutively machined on titanium (right, blue) at -100V. Scale is 100 μm (left) and 200 μm (right). 57
5.5 A schematic diagram of Configuration 1. 59
5.6 SEM image of the copper collector titanium nanoparticle clusters found on copper collector. 59
5.7 A schematic diagram of Configuration 2. 60
5.8 The 'web' of nanoparticles formed between the target sample (left: copper; right: titanium) and the alligator clip connecting the collector sample (left: titanium; right: copper) to the power supply. 61
5.9 A schematic diagram of the configuration used for the electric field experiments. 63
5.10 SEM images showing titanium samples placed in an electric field established between titanium collectors and copper collectors, scale is 1 mm. 65
5.11 SEM images showing copper samples placed in an electric field established between titanium and copper collectors at 500 V. All length scales correspond to 500 μm. 65

5.12 A schematic diagram of the configuration used for the electric charge experiments. 67

5.13 SEM images showing titanium samples (left) placed beneath titanium collectors (right) at +500 V and -500 V. Images of the titanium samples are of 1mm length scale and the collectors have length scale of 10 μm. 68

5.14 SEM images showing titanium samples (left, blue) placed beneath copper collectors (right, red)) at +500 V and -500 V. Images of the titanium samples are of 1mm length scale and the collectors have length scale of 50 μm. 68

5.15 SEM images showing copper samples (left, red) placed beneath titanium collectors (right, blue) at +500 V and -500 V. 69

5.16 SEM images showing copper samples (left) placed opposite copper collectors (right) at +500 V and -500 V. 69

A.1 The assembly of the prototype is shown above 86

A.2 The major components of the glove box are shown above. 90

B.1 An image of the vacuum pump showing the oil mist eliminator at the pump outlet and the rigid tubing leading to the pump inlet. 91

B.2 An image of the VTM and its components. 92

List of Tables

3.1 Criteria for the design of the chamber for laser micro-machining experiments in a controlled environment 17

4.1 Summary of each chamber option and its characteristics 25

4.2 List of parts that were purchased or found and fitted to the prototype chamber 28

4.3 Parameters for regression-fit model relating accumulated pulse intensities and effective line width by Lehr et. al. (2014) 29

4.4 Comparison of the squared line width experimentally found in oxygen, nitrogen and helium with values determined using the regression-fit model by Lehr et. al (2014). Each experimental value is an average of 3 measurements using SEM at 26.1 $\frac{GW}{m^2}$. Each value has a unit of μm^2. 30

4.5 Atomic composition [%] of the polished, unpolished, wiped and helium flow samples. 31

4.6 Laser and scanning parameters for generating nanoripple structures on titanium 34

4.7 Laser and scanning parameters for generating aggregate and chaotic structures on titanium 40

4.8 A summary of the structures generated in nitrogen and vacuum environments using the laser settings known for creating *aggregate* and *chaotic* structures . 41

4.9 Summary of each chamber option and its characteristics after prototype testing 46

5.1 A summary of the trial runs completed at 100 V with varying polarity. . . . 56

5.2 A summary of the results from the experiments using Configuration 1. 58

5.3 A summary of the results from the experiments using Configuration 2. 61

5.4 A summary of the experiments completed at 500 V with target samples place in an eletric field establishd between collectors A and B. 64

5.5 A summary of the experiments completed at 500 V with target samples placed directly below Ti or Cu collector samples of varing polarity. 66

Abstract

Femtosecond (fs) laser micro-machining of metals is useful in imparting surface roughness and wettability characteristics to a material. In fact, extensive research has been done to highlight the relationship between the variety of surface topographies and the resulting wettability characteristics. Recent studies have further explained that wettability can also be linked to surface chemistry, but the nature of this relationship is unclear. Since the surface chemistry of a material is dependent on the machining and storage environment, studies into its impact on surface wettability must be carried out in an environment that effectively isolates the materials from contamination. Hence, this thesis details the design, prototyping and construction of a chamber for fs laser micro-machining in controlled environments.

Home-made and commercially available chamber designs were analysed according to a number of criteria. Using materials that were readily available, a prototype chamber was designed, assembled and tested to determine the limitations of such an apparatus. The cost-benefit analysis of the designed options and the data collected from prototype testing were used to inform the final design choice. A standard operating procedure (SOP) was also prepared to guide future operators in the use of the prototype and finalized chamber design.

During the prototype testing, it became apparent that nanoparticle accumulation in the chamber could occur under certain conditions. Thus, a short study on a novel nanoparticle collection/removal method was conducted. Experiments showed that an electrically charged metal sheet can attract nanoparticles from a surface during laser micro-machining. While there is no indication of a net surface charge on nanoparticles, the results demonstate that voltage and choice of material affect the volume of nanoparticles collected.

Abrégé

Le micro-usinage au laser femtoseconde (fs) est utile pour conférer au matériau des caractéristiques de rugosité de surface et de mouillabilité. En fait, des recherches approfondies ont été effectuées pour mettre en évidence la relation entre la variété des topographies de surface et les caractéristiques de mouillabilité résultantes. Des études récentes ont en outre expliqué que la mouillabilité peut également être liée à la chimie de surface, mais la nature de cette relation n'est pas claire. Étant donné que la chimie de surface d'un matériau dépend de l'environnement d'usinage et de stockage, les études sur l'impact de celle-ci sur la mouillabilité de la surface doivent être réalisées dans un environnement qui isole efficacement les matériaux de la contamination. Par conséquent, cette thèse détaille la conception, le prototypage et la construction d'une chambre dans le but de réaliser un micro-usinage laser dans des environnements contrôlés.

Une combinaison de conceptions de chambre fabriquées à la maison et fabriquées par des professionnels a été analysée selon un certain nombre de critères. En utilisant des matériaux facilement disponibles, un prototype de chambre a été conçu, assemblé et testé pour déterminer les limites d'un tel appareil. L'analyse coûts-avantages des options conçues et les données collectées lors des essais de prototypes ont été utilisées pour éclairer le choix final de la conception. Une procédure standard d'exploitation (SOP) a également été préparée pour guider les futurs opérateurs dans l'utilisation du prototype et de la conception de la chambre finalisée.

Au cours de l'essai du prototype, il est devenu évident que l'accumulation de nanoparticules dans la chambre pouvait se produire dans certaines conditions. Ainsi, une courte étude sur une nouvelle méthode de collecte / élimination des nanoparticules a été menée. Des expériences ont rélévé qu'une tôle métallique chargée électriquement peut attirer des nanoparticules d'une surface lors du micro-usinage au laser. Bien qu'il n'y ait pas d'indication

d'une charge surfacique nette sur les nanoparticules, les résultats démontrent que la tension et le choix du matériau affectent la quantité de nanoparticules collectées.

Acknowledgements

No woman is an island and I am thankful for it. The last two years have been an adventure that I will forever cherish. I matured as an individual and a researcher because of the unwavering support of my supervisors and colleagues.

To my supervisor, Anne, thank you for challenging me to be a better researcher, for guiding me in moments of doubt and for teaching me true dedication. Your passion for research inspired me to go beyond and I am forever grateful that you were my supervisor. Pierre-Luc, thank you for always having time to listen and for setting me on the right path when I was lost.

I'd also like to thank the technicians and support staff of the Department of Chemical Engineering. Thank you to Frank for helping me find the tools I needed and to Gerald for answering my electronics questions. Thank you to Dr. Shang for teaching me everything I needed to know about the XPS, your patience and tutelage are appreciated.

My colleagues made the time fly so quickly. Mike, I'm so happy that our lunchtime crossword sessions have evolved into a great friendship. Your humour and words of encouragement always came at the right time, and I am thankful that I met you. Thank you Evelyne for training me on the VTM and glove box, and always having time to listen to my struggles. Abhi, Adya, Damon, Felipe, Sanchari and Youssef, thank you for making me feel at home in the BSEL group.

None of this would have been possible without the support of my family, especially my mom and brother. Their faith in me and my abilities is beyond my understanding, but I'm blessed to have them in my corner. Last but certainly not least, thank you to my partner in life, Vilhelm. Your love and support mean the world to me.

Chapter 1: Introduction

Laser micro-machining is a contactless, single-step approach that uses a light source to ablate a surface, resulting in imparted roughness. Materials can be treated in a variety of environments because the laser is an adaptable work tool. In particular, femtosecond (fs) lasers are attractive as a machining tool because they balance high intensity with low pulse energy and short pulse duration (Liu et al., 1997). These characteristics result in precise machining with a small heat affected zone (HAZ) which reduces incurred damage to the substrate material (Ahmmed et al., 2014). Studies over the last two decades have elucidated the relationships between laser parameters and imparted surface texture characteristics (Kietzig et al., 2009; Nayak, 2008).

In metals, research shows that after micro-machining, surfaces transition from one wetting state to another following exposure to air (Kietzig et al., 2011; Bizi-Bandoki, 2011). This phenomenon implies that surface wettability is a result of both surface texture and chemistry, and when creating specific wettability properties via lasers, micro-machining and environmental parameters must be controlled. So far, substrates machined in vacuum or gas environments have been analysed in ambient air (Long et al., 2015; Liu et al., 2015; Kim et al., 2016; Bizi-Bandoki et al., 2013; Chang et al., 2010; Geng et al., 2012; Zhang et al., 2016), preventing researchers from understanding which surface chemistry characteristics are attributable to air. The *Biomimetic Surface Engineering Laboratory* (BSEL) at McGill University is experienced in developing surface textured metals and polymers. The group has effectively conducted micro-machining expeirments in air, vacuum and other gas

environments to understand the wettability of surfaces post-machining. Further, the *Plasma Processing Laboratory* (PPL) is well-versed in conducting controlled environment experiments to prevent contamination of polymer samples during plasma surface modification.

The thesis herein describes the design and construction of a controlled environment system for femtosecond laser micromachining and surface chemistry analysis. The body of work includes an experimental study of the capacities and limitations of a prototype chamber to determine the most robust and suitable design for the machining and analytical applications. The methods for constructing and using the final product in tandem with an X-Ray Photoelectron Spectroscopy apparatus (XPS) are also outlined.

Chapter 2: A Review of the Literature

The following is a review of the literature detailing the status of research in understanding the interactions between the environment and target surfaces during laser micromachining. Fundamental principles and techniques related to femtosecond laser micromachining and wettability are briefly discussed.

2.1 Surface Texturing of Metals

When machining a metal target, the energy from the laser is absorbed by the electrons and lattice of the material. As the lattice vibrates, bonds are broken and the material expands, resulting in ablation and restructuring of the surface (Mishra and Yadava, 2015). When the fluence of a laser beam exceeds the threshold fluence of the substrate, material is removed in a process called ablation. Operating at a different fluence will affect how much energy is deposited the surface and consequently, the type of structures generated (Ahmmed et al., 2014).

The fluence (F) $[J/cm^2]$ of a Gaussian beam describes the theoretical energy the substrate experiences per unit area and is calculated according to Equation 2.1 where ω_{theo} is the theoretical beam diameter, f_p is the repetition rate and P is the power of the laser. The repetition rate decribes the number of pulses emitted in one second. During experiments,

the power of the laser beam is locally controlled to change the fluence deposited on the substrate. The energy input from the laser beam onto the substrate can also be described as the intensity (I) [W/cm^2].

$$F = \frac{8P}{\pi(\omega_{theo})^2 f_p} \tag{2.1}$$

Typically, the goal of micromachining is to create a pattern of structures on a sample surface over an area larger than the laser beam diameter. There are two ways to do this: (1) the laser beam travels across the sample with a multi-axis galvanometer or (2) the sample is displaced with a translation stage (Ahmmed, 2015a). Lines and patches are fabricated on substrates at a rate that corresponds to the speed of the galvanometer or translation stage, known as the scanning speed, ν. When using either technique, the spots created by a pulsed laser beam must overlap to create a continuous pattern either as a line or a patch. The overlap of the beam increases the fluence experienced by the substrate so the effective width of the ablated area will differ from the laser beam spot size. The effective beam diameter, ω_{eff}, is the line width on an ablated surface after accounting for the effect of material properties and machining environment on ω_{theo}. Experimentally, ω_{eff} is determined using Scanning Electron Microscopy (SEM) imaging of the sample ablated at the required F, and scanning speed, ν.

During a raster scan, the number of lines (Equation 2.2) required to ablate a patch is derived from the length of the patch, d, the required vertical overlap of pulses to generate a structure, φ_{line}, and ω_{eff}. In the laboratory, the power corresponding to the required F is the primary laser parameter that is set by the user. When machining a patch, the translation velocity of the stage, ν, is set at the controls of the translation stage along with the desired patch dimensions. The total energy the surface experiences is the sum of the individual pulse energies described by a Gaussian distribution. When the pulses are suffiicently overlapped,

a flat top total energy profile is generated, resulting in a homogeneous surface morphology.

$$n = \frac{d}{(1 - \varphi_{line})\omega_{eff}} \tag{2.2}$$

2.1.1 Accumulated Fluence

In a single spot, the ablation threshold of a material changes in relation to the number of pulses applied in accordance with the accumulation model (Brikas et al., 2008). When a line is scanned, depending on the pulse overlap, a subsequent pulse will interact to varying degrees with molten, re-solidified or structurally different material at the target surface. When making a patch, the subsequent line is scanned several seconds later, so the laser pulse will interact with re-solidified molten material. In both cases, the thermal and absoprtion properties of the material have changed, so the surface can be ablated at a fluence below the ablation threshold. By extension, a glass window or lens may be ablated after multiple uses with a laser even if the fluence is below the material's ablation threshold. The accumulated fluence or intensity of spots is the sum of the energies experienced by a substrate after mutiple pulses in a line ($F_{pulse-acc}$ or $I_{pulse-acc}$) or multiple lines on a patch ($F_{line-acc}$ or $I_{line-acc}$).

2.1.2 Structures & Wetting Properties

The main goal of most laser micro-machining efforts is to influence wettability by changing the surface roughness of a material (Bhattacharya et al., 2008; Baldacchini et al., 2006). The structures generated on a metal or polymer sample surface can be self-assembled or directly inscribed depending on the fluence of the beam. There are two main types of structures created from laser ablation: laser-inscribed structures and laser-irradiated structures. Laser-inscribed structures are many in variety and are of micro-scale length. They tend to be periodic geometric patterns including parallel grooves, columns and square pillars; and

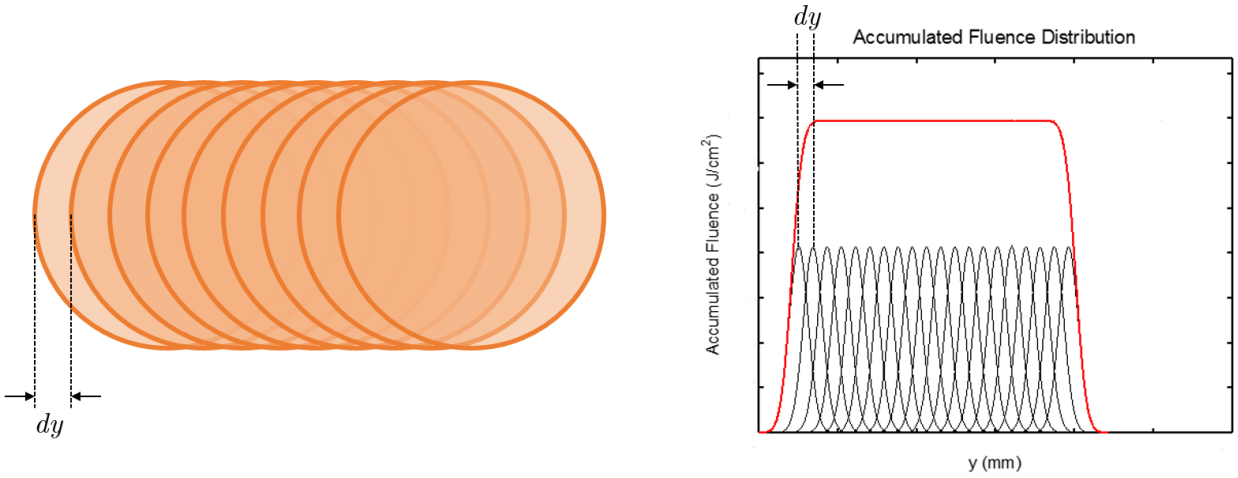

Figure 2.1: The gaussian profile of the laser beam at each spot is shown to overlap, resulting in the surface experiencing an accumulated fluence over the line.

they require high fluence to generate ablation widths equal to or larger than the effective beam diameter (Ahmmed, 2015a). Laser-irradiated structures include random structures and laser induced periodic surface structures (LIPSS) that are typically nano-scale length range. LIPSS can be manufactured independently or observed as nano-scale decoration on other structures, whether irradiated or inscribed. Generally, laser-inscribed structures are specific patterns directly ablated by the laser while laser-irradiated structures are indirectly generated as a result of the laser, scanning, and environmental parameters.

The resulting wetting properties of the sample surface depend on the intrinsic properties of the material and the texture that has been induced or inscribed on the surface. In the Wenzel wetting theory (Figure 2.2(b)), metals which tend to be hydrophilic, will become *more* hydrophilic upon *roughening* with a laser (Wenzel, 1936). According to the Cassie wetting theory (Figure 2.2(c)), one would expect that columnar structures such as square pillars and hierarchical structures like microscale bumps covered with nanoscale ripples would be hydrophobic (Courbin and Stone, 2007; Seo et al., 2015). This is because the raised pillars and nanoscale ripples allow for air trapping between a water droplet and the surface (Johnson

and Dettre, 1964).

Research shows that the reality is exceedingly less precise (Extrand, 2003). The sample material, roughness and processing parameters such as machining/storage environment and gas pressure will further influence the final wetting properties of the surface (Bizi-Bandoki et al., 2013; Kietzig et al., 2011). In fact, recent studies show that the final wetting properties of a laser micro-machined surface are a result of both surface roughness and chemistry.

2.2 Surface Chemistry and Wetting Transition on Laser Textured Metals

When characterizing the wettability of surfaces, an apparent contact angle can be calculated at the contact line using the sessile drop method. It is a visual procedure, where a droplet is released from a syringe onto a surface and the motion is recorded on a camera, which is part of the goniometer used to measure the angle (Zorba, 2008; Zorba et al., 2006; Kietzig et al., 2009; Kietziga et al., 2011; Jagdheesh et al., 2011). The view of the droplet is a side profile that allows the measurement of the apparent contact angle as shown in Figure 2.2(a).

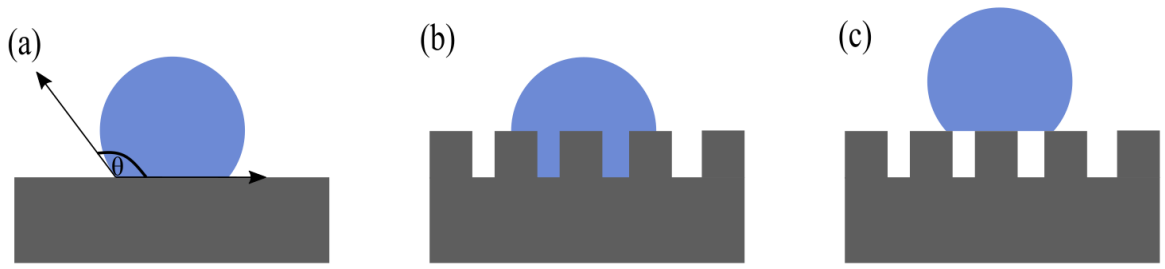

Figure 2.2: (a)The typical view of a water droplet on a flat surface where θ is the contact angle measured , (b)A Wenzel wetting state where a hydrophilic surface becomes superhydrophilic upon *roughening*, (c)The Cassie wetting state where air is trapped between the water droplet and the *roughened* surface.

Recent studies indicate that the measured contact angles are only a snapshot of the

possible wettability behaviours a surface can exhibit (Ling et al., 2016; Yin et al., 2011; Geng et al., 2012; Kietzig et al., 2009; Bizi-Bandoki et al., 2013). In fact, the literature shows that the environment in which a substrate is fabricated and stored will affect its wetting characteristics. Temperature and type of gas are among the environmental parameters that have been found to influence substrate wettability. In a case demonstrated by Ling et. al., as a hydrophobic surface with Cassie state wetting properties is cooled from 20 °C to 0 °C, it transitions to a metastable Cassie state where the droplet sags and the liquid-solid interface increases (Ling et al., 2016). Another study by Yin et. al. (2011) showed that at high relative humidity (above 60%), as the surface temperature approaches the dew point temperature and condensation occurs more often, there is increased wettability and a transition from Cassie to Wenzel state (Yin et al., 2011). The process was proven reversible - leaving the samples at room temperature for days in low humidity restored the superhydrophobic property (Yin et al., 2012). In submerged experiments, micromachined Cassie state surfaces irreversibly transitioned to Wenzel state when high pressure was applied to the water (Lei et al., 2010; Rathgen, 2010).

Further, the gas environment during and after surface treatment influences the wettability properties of metal surfaces. This is characteristic for laser micro-machined as well as electrically and chemically treated metal surfaces following storage in air (Kietzig et al., 2009, 2011; Long et al., 2015; Liu et al., 2015; Kim et al., 2016; Bizi-Bandoki et al., 2013). In some instances, the metal surfaces evolve from super-hydrophilic to super-hydrophobic (Chang et al., 2010; Geng et al., 2012). Chang et. al. (2010) and Geng et. al. (2012) noted that this behaviour on copper nanowires and nickel micro-nano cone arrays may result from the formation of oxide compounds on the surface over the course of 30 days. Other researchers have indicated that the wettability transition of metal surfaces after fs micromachining is a result of an increase in adsorbed organic compounds, including C-H, C-C and C=C hydrocarbons (Long et al., 2015; Liu et al., 2015; Zhang et al., 2016).

Generally, researchers acknowledge that a change in surface chemistry is the reason for the wettability transition in metals. The debate lies in the mechanism of wettability transition. Kietzig et. al. (2009 & 2011) attributed the transition of fs micromachined metal surfaces from hydrophilic to hydrophobic wettability after a few days to the decomposition of carbon dioxide into carbon (Kietzig et al., 2009, 2011). Bizi-Bandoki et. al. (2013) found similar behaviour but reported the cause as an increase in non-polar carbon groups and a decrease in water molecules in other cases (Bizi-Bandoki et al., 2013). Beyond wettabilty, Lehr et. al. (2014) has shows that the processing medium and pressure affects the surface characteristics such that the machining parameters must be tuned to deliver the same texture in different gases (Lehr et al., 2014).

The bottomline is that the structure of the machined metal surface does not change following laser irradiation, hence the change in wettability is a result of changes in surface chemistry. Moreover, wettability can possibly be controlled by tuning surface chemistry and texture, but the specific relationship between processing gas and observed wettability is still unknown. There is currently no consensus as to when the surface reactions begin, how the processing environment affects the reactivity of the surface and what the micro- and nano-scale surface-water interactions are at the contact line. To better understand this, the processing and analytical environment must be completely isolated from the ambient environment. This requires a new system that is compatible with the necessary apparatuses for micromachining and surface chemistry analysis.

2.3 Controlled Environment Apparatus

Literature on femtosecond laser micro-machining in gaseous or vacuum environment focuses heavily on the effect of processing parameters on the resulting texture but not the chemistry. Hence, there has been little incentive to create a system to control the processing and analytical environment. In the past, experiments in gas environments were carried out in ambient

environment with a gas nozzle directed on the substrate surface. Following machining, the substrates were exposed to the ambient environment for necessary analysis (Robinson and Jackson, 2006; Perrie et al., 2004). Chambers were later introduced for vacuum and gas environment experiments (Husinsky et al., 2016; Michel et al., 2007; Lehr et al., 2014). During such experiments, the samples were irradiated with a laser beam traveling through the chamber window. While Husinsky et. al. (2016) and Museur et. al. (2007) used stationary substrates for single and multiple pulse experiments, Lehr et. al. (2014) used a chamber equipped with a 3-D translation stage to manipulate the sample in three directions (x, y, and z). In all three cases, the samples were removed from the chamber and exposed to ambient air for storage and transfer to SEM and/or XPS apparatuses for analysis.

In a completely isolated environment, the laser beam would travel through a window before hitting the target substrate. Experiments may be conducted under gas or vacuum, after which the substrate must be transported to the analytical apparatus without exposure to the ambient environment. Hence, the interaction of the laser beam with the window, the immediate environment surrounding the substrate in the chamber and the opportunities for sample contamination must be well understood.

2.3.1 Interaction of fs Laser Beams with Glass

As a laser beam travels to the target substrate through a window, the refractive index of the glass might change. Typically, the refractive index of a material increases or decreases upon changes to its crystal structure and generation of defects. Krol et. al. found that an increased in 2- and 3- membered ring structures in the fused silica network led to a densification of the sample and was responsible for an increase in refractive index (Krol, 2008). This type of modification depends on the laser repetition rate, fluence and wavelength. It is also dependent on the glass composition which typically controls the process by which energy dissipates in the material. Krol found that the refractive index in fused silica increases

while in phosphate glass it decreases under the same processing parameters (Krol, 2008). Interestingly, Siiman et. al. also found that similar structural changes which result in the increase or decrease in refractive index can be achieved without laser induced damage (Siiman et al., 2009). A change in the refractive index of a glass window influences the beam characteristics, specifically the ω_{theo}, on the target substrate. Simultaneously, thermal loading from the laser beam as it passes through the glass will change the structure of the material which could change the shape of the laser beam. Dust and other particles can also create localized heating zones and diffracted light upon interaction with the beam (Ion, 2005).

Figure 2.3 shows the extension of a beam (pink line) through a borosilicate glass window with thickness of 1.6 mm. The refractive index, n, the incident angle of the beam on the glass window, α, and the glass thickness, t, are the key parameters when calculating the new theoretical beam radius (Equation 2.3), $\omega_{theo,new}$, of a laser beam through glass.

$$\omega_{theo,new} = t \times \tan\alpha \times (1 - \frac{1}{n}) \tag{2.3}$$

2.3.2 Gas, Plasma and Particle Environment

Figure 2.4 shows that during ablation, there are 3 regions in the volume above the target space: (1) the gas environment, (2) the ablation plasma and (3) the particle cloud (Lehr et al., 2014). In a closed environment surrounding the substrate, the effects of these 3 regions on the resulting structures may become more pronounced. Specifically, transparent media like gases cause a fs laser beam, with fluence greater than 10^8 GW/m^2, to self-focus in a phenomenon known as the Kerr effect (Lehr et al., 2014; Bergé et al., 2007). The electromagnetic field of the laser beam increases the refractive index of the transparent medium, which causes the intensity of the beam to increase at the centre, i.e. the beam self-focuses. Simultaneously, the laser beam ionizes the gas molecules through multi-photon

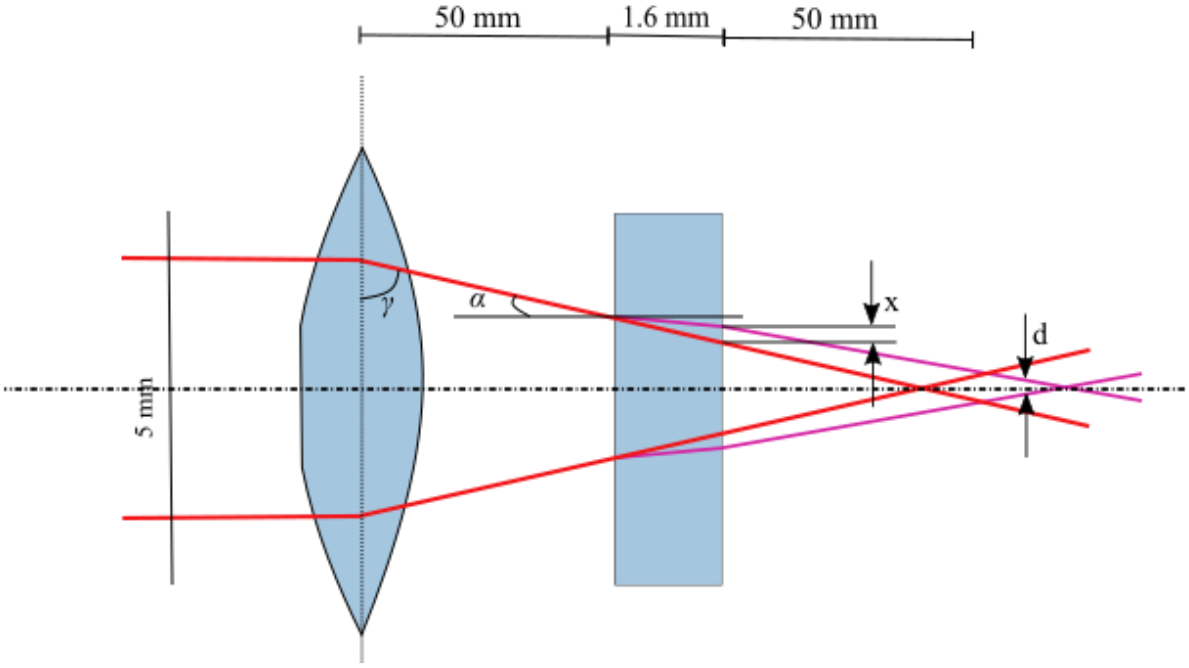

Figure 2.3: Passing a laser beam through the glass results in an increase in beam diameter. In this image, the focusing lens has a focal length of 100 mm.

absorption and avalanche ionization, resulting in plasma formation. The plasma grows to a critical density that makes it opaque, thus reducing its refractive index and countering the Kerr effect. Therefore, the focus/defocus cycle affects the experienced pulse fluence and wavelength at the target surface. Further, different gases will generate plasma with differing refractive indices, so effects will vary.

The particles removed from a substrate are vaporized by the heat of the laser beam and form a cloud above the material that may interact with the laser beam if it expands at a rate slower than the duration between incoming pulses. The plume can also form an ablation plasma if the laser electric field is above its threshold for optical decay, which happens at high fluence. During an experiment with a fs laser beam at $f_p > 10$ kHz, the plasma grows to a critical density at which it behaves like a shield as it adsorbs the laser irradiation. Particles removed from the surface have a similar effect as they reduce the fluence experienced at the target surface. (Zhukov and Bulgakova, 2009; Cheng et al., 2013)

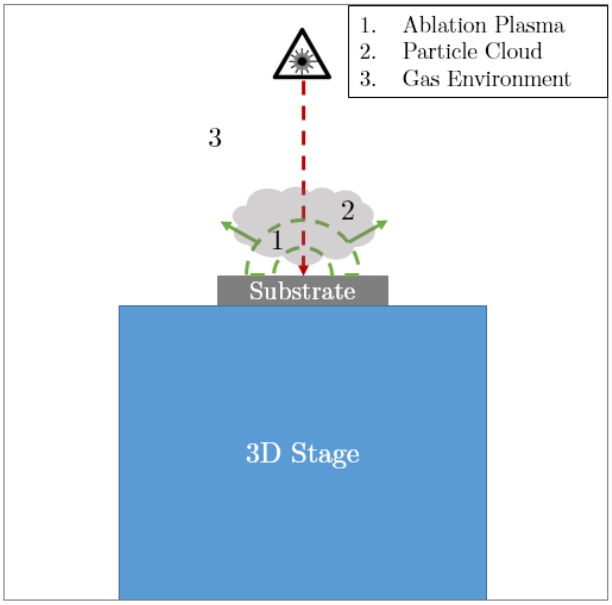

Figure 2.4: The interaction of a laser beam with the gas environment, the expanding plasma and the particle cloud. Adapted from Lehr et. al. (2014)

2.3.3 Substrate Interaction with Environment

Following a laser micro-machining experiment, a sample is typically transported to the necessary apparatuses for analysis. XPS and SEM are two common analytical tools used for surface topography and chemistry analysis, respectively. The transfer process to an analytical apparatus poses a contamination risk by the ambient environment.

XPS is used to investigate the elemental composition of the substrate after machining. Thus, the integrity of the *initial* resulting surface chemistry from micromachining must be maintained in order to obtain accurate results. XPS analysis occurs under vacuum in a complex apparatus whose entry port only accomodates custom sample holders. This means that samples must be transferred to a special sample holder in order to be accepted by the XPS apparatus. Samples that are sensitive to the ambient environment can be transferred to a vacuum transfer module (VTM) in a glove box environment. The VTM is a special device created by Thermo Fisher Scientific for the K-Alpha XPS apparatus. It fits directly into the apparatus entry port and has been used by the Plasma Processing Laboratory for

protection of sensitive samples from the ambient environment before XPS analysis.

SEM is an analytical tool used to visualise the topography of a laser micro-machined surface, while under vacuum. The topography of a substrate remains constant after micro-machining, so samples can be exposed to the ambient environment without affecting SEM results. Nevertheless, a sample with an abundance of nanoparticles can negatively affect the function of the vacuum pump in the SEM apparatus. If the pump is unable to achieve a vacuum environment, the system will not work. Typically, samples are sonicated in a solvent before SEM analysis to remove debris and nanoparticles. In a situation where the original surface chemistry is under investigation, the samples should be sonicated after XPS analysis. Nonetheless, physical characteristics such as height and width of generated structures can inform procedures like depth analysis during XPS analysis.

During experiments in ambient environment, a vacuum hose is used to remove nanoparticles generated on the substrate. In a gas environment with no outflow, the nanoparticles will accumulate on the substrate (Ahmmed, 2015b; Lehr, 2015; Lehr et al., 2014). Some studies have used a laser pulse to generate a shock wave on the rear side of a sample to detach nanoparticles. The procedure is advantageous because it ensures that further damage is not incurred to the front side of the substrate but it is a challenging process to implement after laser micromachining (Merkt, 2008; Murthy Peri et al., 2011; Leiderer et al.). Recent studies have suggested that nanoparticles may have electrical properties, specifically surface charge (Barbosa et al., 2016; Ivlev et al., 2003; Li et al., 2009; Watanabe, 2006; Wang et al., 2014). However, there is no indication as to whether nanoparticles generated during laser micro-machining exemplify this characteristic. If nanoparticles are charged species, the surface charge can be used to manipulate nanoparticles out of a system as a removal method. As an alternative, if the typical height of the generated structures are known through SEM, depth analysis of the substrate surface using the XPS apparatus can aid in the understanding of the surface chemistry beneath accumulated nanoparticles.

In conclusion, a controlled environment system for laser processing and surface chemistry analysis must be compatible with the XPS apparatus of choice and include a process by which nanoparticles are removed from the surface of the substrate.

Chapter 3: Objectives

As demonstrated by the literature review, the necessary step to explore the relationships between machining environment and a substrate's surface chemistry is the development of a controlled environment for laser micromachining environments and surface chemistry analysis. More explicitly, the objectives of this thesis are:

1. *Propose designs and experimental processes based on available technologies and criteria*

   The chamber design for micromachining experiments must be equipped for vacuum and gas environments (N_2, He, Ar), and compatible with the Coherent Libra Ti:Sapphire (800 nm; 150 fs) femtosecond laser with average output power of 4W. The proposed options fulfilled the basic criteria described in Table 3.1. CADs and schematics of the chamber options were prepared; the designs included home-made chambers and a custom-fitted VTM.

2. *Build a prototype chamber and complete design testing*

   Thermo Fisher Scientific clarified that determining the feasibility of a design for a custom-fitted VTM would require months. In the meantime, a prototype chamber was assembled to determine the capacities and limitations of a home-made design. The prototype was tested in gas and vacuum environment conditions for line and patch scanning on titanium. The results were analysed using XPS and SEM. The process for preventing exposure of the sample to the ambient environment included the use of the VTM since the K-Alpha XPS apparatus is readily available at McGill University.

Using a prototype to complete typical controlled environment experiments highlighted the time cost, design faults and necessary accessories to properly choose the final design and improve on it.

3. *Create Standard Operating Procedures (SOPs) for all equipment and processes required for typical controlled environment experiments*

   Taking lessons from the prototype testing, SOPs were prepared to guide future users on the appropriate ways to operate the prototype chamber and final design chamber, and procedures for sample loading, unloading, storage and transfer before analysis in the XPS apparatus. Further, observations of the gas environment on laser settings and the accumulation of nanoparticles were recorded.

Table 3.1: Criteria for the design of the chamber for laser micro-machining experiments in a controlled environment

Criteria	**Details**
Power	Glass material must withstand maximum of 500 mW
Wavelength	Laser beam operates at wavelength: 200 - 800 nm
Supports gases (N_2, He, Ar)	Compatible Swagelok fittings to ensure gas flow
Supports vacuum	Vacuum pump with KF-25 ports
Space requirements	Space between 100 mm lens and 3-D stage - L: 9.8 cm W: 7.6 cm; Glove Box Entry Port- D: 16 cm L: 42 cm
Fix to the stage	Use screw holes in stage
Weight	<3.8 kg (Load capacity of z-axis stage with x- and y-axis stages)

Chapter 4: Chamber Design & SOP Development

4.1 Designs for a Controlled Environment Chamber

In general, the chosen design will be loaded with a sample or multiple samples and placed directly on the 3-D translation stage. The chamber will be connected to one of 2 gas lines that are already existent in BSEL and/or to the vacuum pump. After an experiment, the gas and/or vacuum lines must be disconnected before the chamber is transported to the glove box in the PPL. Once in the glove box, the sample(s) will be unloaded from the chamber and placed in the VTM for transfer to the XPS.

A set of criteria (Table 3.1) was developed to guide the design process. The most important restrictions apply to the glass which must withstand up to 500 mW from the laser beam and wavelengths between 200 and 800 nm. Upon contact with a glass window, the laser beam will bend away from the axis due to the change in refractive index. A window with a higher refractive index will result in less bending. The chamber itself must support gas, most importantly, N_2, He and vacuum environment; this criterion will direct the choice of fittings attached to the chamber. Finally, the physical dimensions of the chamber are important to prevent damage to the 3-D translation stage and lens while ensuring access through the glove box transfer port.

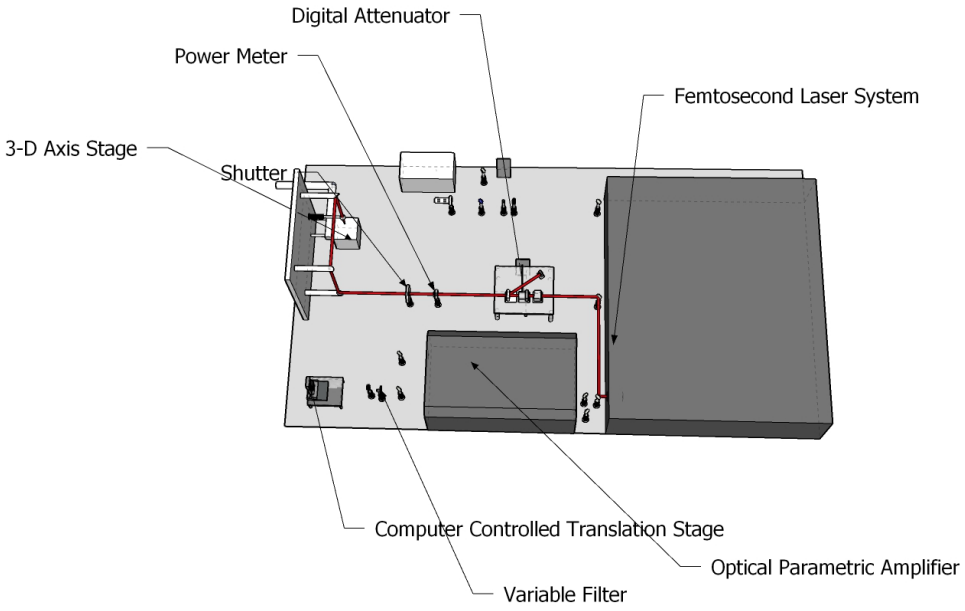

Figure 4.1: An illustration showing the laser beam path (in red) from the fs laser system to the 3-D axis stage.

4.1.1 Design Considerations

Lens

The laser beam refracts when it travels through the glass window thus changing the beam diameter to $\omega_{theo,new}$ as shown in Equation 2.3. The input beam diameter, $\omega_{theo,old}$, is 5 mm, the focal length of the lens is 100 mm. The 100 mm lens is the most frequently used lens in the BSEL for experiments on the 3-D axis stage. A 200 mm focal length lens is also available, but the chamber was designed for the more limiting 100 mm lens to ensure that it is compatible with both options.

Physical Dimensions

The space between the 3-D axis stage and the lens measured 9.8 cm. This is the maximum amount of space available to accomodate the chamber when mounted on the stage. The

entry port of the glove box (MBRAUN MB200B) contains a transport tray with a width of 14 cm and a length of 37 cm; the maximum height of any object placed in the entry port must be less than 12 cm. Thus, the total length of the chamber and any attached accessories that are necessary for sample transport must be less than 37 cm, assuming that the height and length are less than 12 cm. The laser table is depicted in Figure 4.1.

The rotary vane vacuum pump (Alcatel 1004A, single-stage vane) available in the BSEL lab flows air or gas out of a system at a rate of 5 $\frac{m^3}{h}$. Ideally, the pump must draw enough air from any of the proposed systems to reach vacuum in less than a minute, so the chamber volume must be less than 0.08 m^3 .

Maintaining a reasonable combined weight of the chamber and added parts is important to ensuring the safe and proper function of the 3-D axis stage. The 3-D translation stage comprises of 3 stages that move in the x-, y- and z-axis respectively. The x- and y-axis stages are the Newport XMS50 model each weighing 2.5 kg with load capacities of 100 N. The z-axis stage is the Newport MVN80 model and it weighs 3.2 kg with a load capacity of 111N. The actuator for the z-axis stage is the Newport LTA-L model with a weight of 0.4 kg and a load capacity of 100 N. The actuator is attached to the z-axis stage and will not move the stage vertically at loads higher than the capacity. The stages are assembled on top of each other, with the x-axis stage on the bottom, the y-axis in the middle and the z-axis on the top. Hence, the load on the x-axis stage includes the two stages it carries and a metal plate that connects the stages estimated to weigh 0.3 kg. Using Newton's 2^{nd} law of motion and assuming acceleration due to gravity ($a = 9.8\ \frac{m}{s^2}$), the total weight carried by the x-axis stage is 6.4 kg, corresponding to a load of 62.8 N (Equation 4.1). The remaining weight that can possibly be carried by the stage without damage is 3.8 kg (Equation 4.2. This is the maximum weight of any apparatus that would be mounted on the 3-D stage. In the event that the apparatus is heavier, the z-axis stage may be removed to reduce the load

on the x-axis stage.

$$Load_{x-axis} = ma \tag{4.1}$$

$$Max\ Weight = \frac{Load\ Cap - Load_{x-axis}}{9.8\ \frac{m}{s^2}} \tag{4.2}$$

4.1.2 Design Options

Four chamber designs were created and compared according to specific characteristics: physical dimensions, cost and mounting options (Table 4.1). Three of the options were designed from vacuum chamber connections that can be supplied by Kurt J Lesker, a company that specialises in vacuum products. The fourth design was a modification of the VTM produced by Thermo Fisher Scientific for the K-Alpha XPS apparatus.

The window options available from Kurt J Lesker for both conflat (CF) and Klein (KF)flanges were kodial (borosilicate), quartz and sapphire glass in ascending order of price. All the glass options were suitable for the wavelength range of the laser so the cheapest and most expensive options were considered for the designs: borosilicate glass (Kurt J Lesker, QF25-100VP) ($n = 1.49$) and sapphire glass (Kurt J Lesker, VPZL-275SW) ($n = 1.77$). Using Equation (2.3), $\tan\alpha$ corresponds to $\frac{\omega_{theo,old}/2}{100mm+1.16mm}$ thus the calculation for the new beam diameter fitted with borosilicate glass is 23 μm and 41 μm with sapphire glass.

It is important to note that the weights of the choices does not include accessories. All the home-made options would require clamps, o-rings or gaskets for all the port connections and Swagelok® fittings for the gas line. These items are included in the cost estimates.

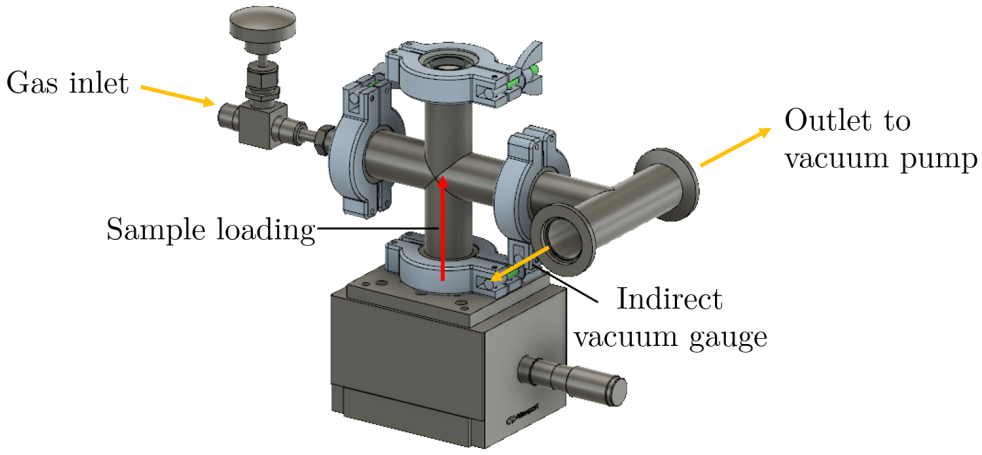

Figure 4.2: CAD illustration of the 4-way Cross Chamber

Option 1: 4-Way Cross

Description: The 4-way cross (Kurt J Lesker, QF25-100-X) has four ports protruding from a central node (Figure 4.2). A tee port would be added to the left-side port such that the vacuum pump and an indirect vacuum gauge could be connected to the vacuum line in order to take pressure measurements. Gases would be fed into the system through the right-side port. A mass flow controller or rotameter could be added to the gas line to control and monitor the flow rate of gases into the system. Samples can be loaded from the bottom port and the glass window fitted to the top port. The 4-way cross measures 10 cm in height and width, with KF25 flange sizes. The cross would be mounted onto the stage by welding a bolt to the bottom flange which will screw directly into the 3-D axis stage. The 4-way cross weighs 0.2 kg.

Option 2: 5-way Cross

Description: The 5-way cross (Kurt J Lesker, QF16-075-5X) (Figure 4.3) measures 5 cm in height with 4 ports extending from the centre and one port extending upwards. The top port would be used for the chamber window and each of the ports would individually service

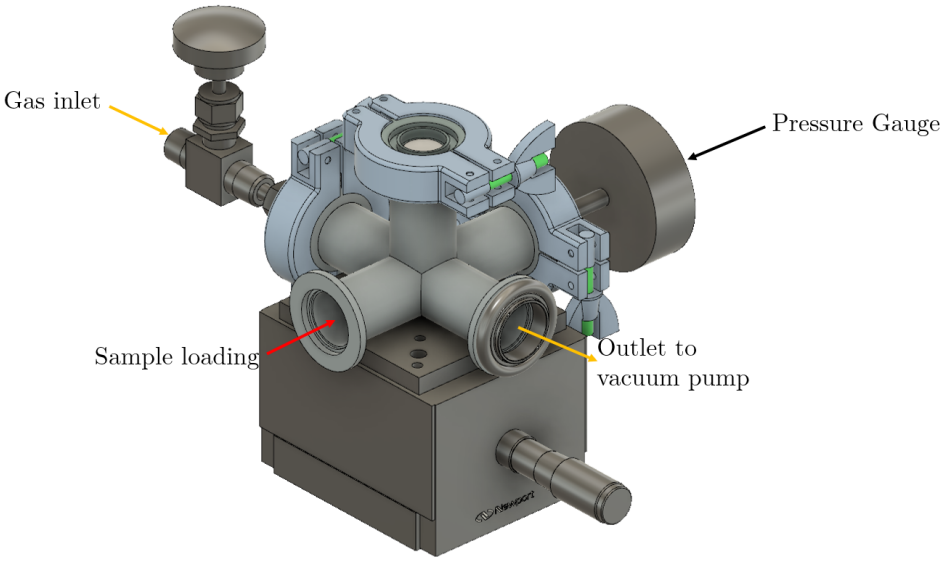

Figure 4.3: CAD illustration of the 5-way Cross Chamber

the gas line, vacuum line, pressure gauge and sample loading. Each sample would be placed flat at the centre of the chamber. The chamber would be mounted to the stage using 3-D printed posts that fasten to the 3-D stage and secure each corner of the chamber. The 5-way cross would be obtained with KF16 flange size and would weigh 0.2 kg.

Option 3: Cube

Description: The cube (Kurt J Lesker, CU6-0275) (Figure 4.4) is 9.4 cm in height with a flange on each of its 6 sides. It would be mounted using a 3-D printed circular holder that fastens to the 3-D stage. Since borosilicate glass is not available in this flange size, a sapphire glass window (view diameter: 1.44 inches) would be fitted to the top side port. The left- and right-side ports would transport gas in and out of the chamber, respectively. The cube will require conflat flanges (CF) instead of the Klein flange (KF) so each port would be secured with a gasket. The front port can hold a pressure gauge while a rotameter can be included on the gas line for more accurate control of the gas environment in the chamber. The bottom port can be used to load samples. The cube is the heaviest option weighing 1.2 kg.

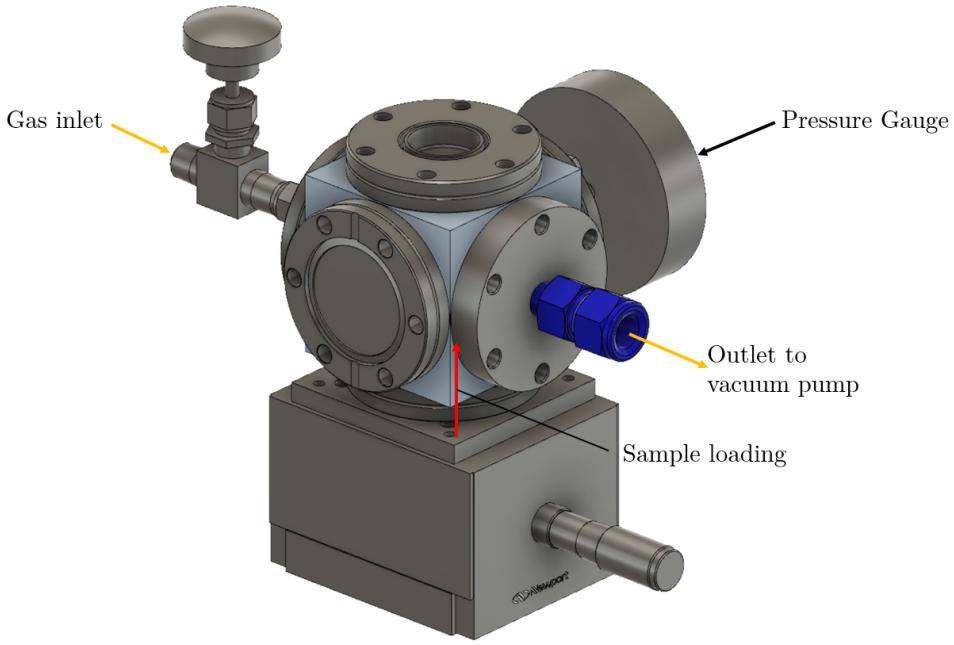

Figure 4.4: CAD illustration of the Cubic Reactor

Option 4: VTM modification

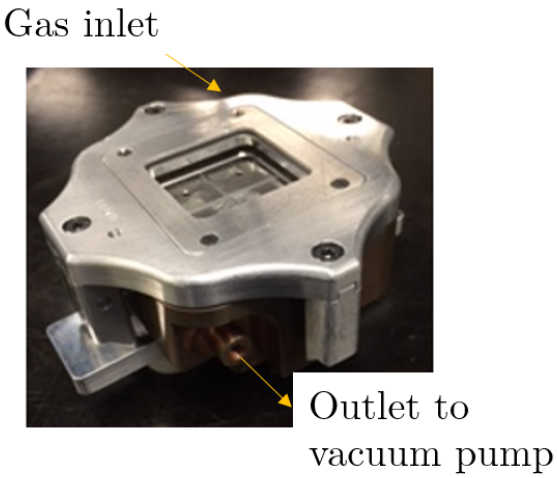

Figure 4.5: An image of the VTM showing the one-way valve for vacuum and glass window

Description: The current design of the VTM (Figure 4.5) includes an outlet port that contains a one-way valve for removing air from the device. The proposed modifications were an inlet port opposite from the outlet to create gas flow in the VTM and replacing the

window with glass that is suitable for laser micromachining. The VTM weighs 0.6 kg and has a height of 4.2 cm, width of 9.1 cm and length of 8.4 cm. Since the VTM is flat, it will not require mounting to the 3-D axis stage. This option would not require the use of a glove box since the VTM is specfically manufactured for the XPS K-Alpha apparatus.

Table 4.1: Summary of each chamber option and its characteristics

	4-way Cross	**5-way Cross**	**Cube**	**VTM**
Cost	$541	$725	$2820	n/a
Height	100 mm	50 mm	94 mm	40 mm
Width	100 mm	80 mm	94 mm	91 mm
Weight	0.2 kg	0.2 kg	1.2 kg	0.6 kg
Mount	screw	posts	holder	none

The VTM modification appeared to be the most elegant option so efforts were made to obtain a quote for the cost of modification. A local machine shop estimated that drilling into the VTM to create an inlet port for gas flow would cost about $300 but the parts required to ensure gas flow were proprietary and difficult to obtain. Hence, Thermo-Fisher Scientific would have to make the modification. While the manufacturer suggested that the modifications were possible, they also clarified that receiving approval and developing a design would take months. In the meantime, a 4-way cross and Swagelok-fitted KF-25 flange were readily available from the PPL, so a prototype chamber could be assembled to enable the design and SOP development process.

4.2 Prototype Chamber & SOP Design

4.2.1 Prototype Chamber

The 4-way cross consists of 4 cylindrical tubes welded at the centre with inner diameters of 1.04 inches or 2.64 cm, hence the estimated volume of the cylinder is $9.301 \times 10^{-5} m^3$.

Since it was too tall, the cross was trimmed and welded to 7 cm to accommodate parts that would attach to the top and bottom ports. Figure 4.2 & 4.6 show that the Kodial (borosilicate) glass window is connected to the prototype chamber at the top port. The glass was chosen for its low cost, which was suitable for a prototype. The bottom port was fitted with a modified blank flange. A screw was welded at the centre of the flange so that when clamped to the 4-way cross, the entire piece fastened into the 3D-axis stage. The left-side port of the 4-way cross is connected to a flange with a 1/4" tube adapter, 1/4" union (Swagelok, SS-4-TA-1-4 & SS-400-6) and a valve (Swagelok, SS-1VS4) for a gas line. The right side would connect directly to the vacuum pump via a KF-25 metal hose; flow to the pump was controlled with a butterfly valve (Kurt J Lesker Company, KBV010MSQF25). Samples were loaded into the chamber from the bottom port. The cross weighed 0.2 kg and the heaviest part added to the assembly was the butterfly valve (0.5 kg) to control flow to the vacuum pump. The total weight of the assembly including clamps, o-rings, valves and the glass window was 1.3 kg. The prototype is less than half of the maximum load capacity so it was not expected to hinder the function of the stages. During all experiments, the rotary vane vacuum pump (Alcatel 1004A, single-stage vane) was switched on to prevent the accumulation of nanoparticles within the chamber.

A makeshift stage of LEGO® was attached to the inside of the bottom flange to a height that corresponded to the focus position of the lens while ensuring that the gas would flow directly over samples.

The 4-way cross chamber modified with the external accessories (valves, window and

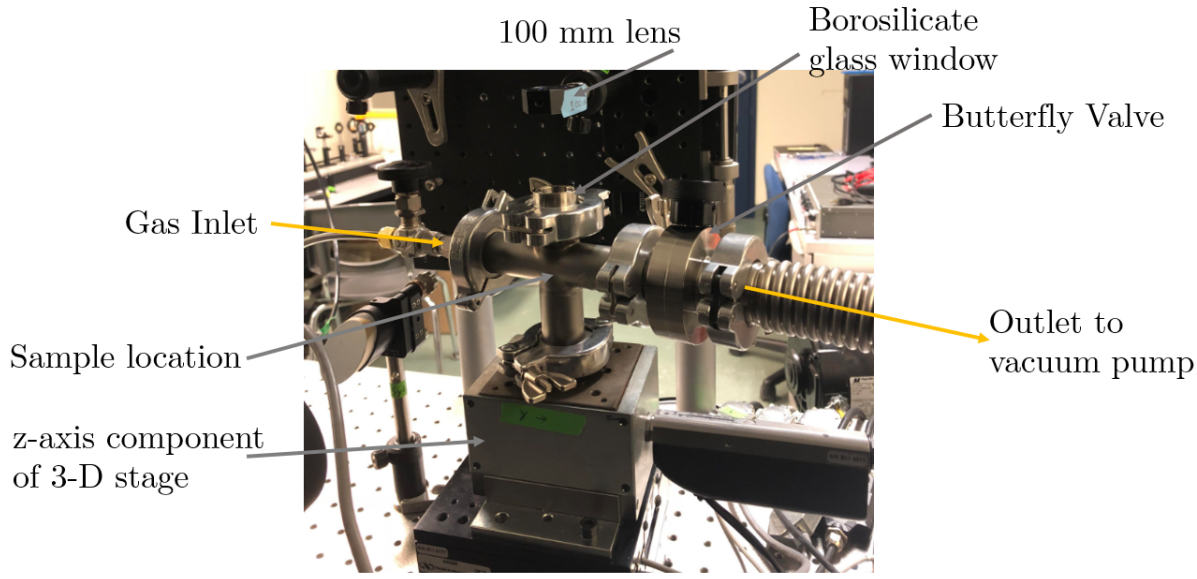

Figure 4.6: An image of the prototype chamber fastened to the 3-D axis stage and connected to the gas and vacuum lines during an experiment.

stage fitting) is physically acceptable for the application of laser micromachining. Next, proof of concept experiments were carried out to determine if the prototype could deliver a controlled environment.

4.2.2 Proof of Concept Experiments

After assembling the prototype, proof of concept experiments were conducted to ascertain that the prototype worked as designed and to determine sample preparation techniques that would improve the surface chemistry analysis procedure. Lines were machined on titanium (99.9% purity, McMaster-Carr) in helium, nitrogen and oxygen to compare with effective line widths found at similar pulse-accumulated intensities by Lehr et. al. (Lehr et al., 2014). This was chosen as the comparison literature because the experiments were also conducted on the same metal and in the same gases. In our prototype chamber, the lines were ablated at a power of 25 mW and a scan speed of 4.2 mm/s. The laser had a repetition rate of 1

Table 4.2: List of parts that were purchased or found and fitted to the prototype chamber

Part	**Supplier**	**Part #**	**Cost**
4-way Cross	Kurt J Lesker	QF25-100-X	available
Kodial Glass Window	Kurt J Lesker	QF25-100-VP	$139.05
Butterfly Valve	Kurt J Lesker	KBV010MSQF25	$361.80
KF25 Flange	Kurt J Lesker	QF25-100-SB	available
Clamps	Kurt J Lesker	QF25-100-CS	available
1/4" tube adapter	Swagelok	SS-4-TA-1-4	available
1/4" union	Swagelok	SS-400-6	available
Ball valve	Swagelok	SS-1VS4	available

kHz and a theoretical beam diameter of 23 μm.

For surface chemistry analysis via XPS, patches at the same laser settings were machined in the prototype on titanium (99.9% purity, McMaster-Carr) in nitrogen and then transferred to the vacuum transfer module (VTM) in a glove box (MBRAUN MB200B) to prevent exposure to the ambient environment. The VTM is built by the same manufacturer (Thermo Fisher Scientific) as the K-Alpha XPS apparatus to protect sensitive samples before XPS analysis. The sample was polished with 200, 400 and 600 grit sandpaper (Silicon Carbide, Anamet Corporation) and sonicated for 10 minutes in acetone before the experiments commenced. The unpolished sample was machined and transferred under the same conditions to compare the atomic compositions on the surface.

Line Width Comparison

The pulse-accumulated intensity ($I_{pulse-acc}$) at the chosen laser settings was 26.1 $\frac{GW}{m2}$. Lehr et. al. (2014) found that the squared effective beam diameters ω_{eff}^2 could be related to the

$I_{pulse-acc}[\frac{GW}{m^2}]$ by the regression-fit model in Equation 4.3, where the regression parameters are shown in Table 4.3. The R^2 for the model was 0.97 for oxygen and helium, and 0.88 for nitrogen (Lehr et al., 2014).

$$\omega_{eff}^2 = \beta_0 \ln I_{pulse-acc} + \beta_1 \tag{4.3}$$

Table 4.3: Parameters for regression-fit model relating accumulated pulse intensities and effective line width by Lehr et. al. (2014)

	Oxygen	**Nitrogen**	**Helium**
β_1	933.03	1272.07	1754.30
β_0	-496.10	-704.31	1250.30

Table 4.4 shows the ω_{eff}^2 values obtained using the model and those found experimentally. Similar line widths are found when comparing the model to the experimental values for lines machined in nitrogen. In the case of helium, the graph provided by Lehr et. al. (2014) visually demonstrates that at 26.1 $\frac{GW}{m^2}$, ω_{eff}^2 should approximately be 4300 μm^2 but the model generates a value of 6972.7 μm^2. The discrepancy between the model and the graph in the paper may be due to a typographical error in the data presentation, because when the β_0 parameter is negative, the model fits the attributed graph more closely (4472 μm^2 at 26.1 $\frac{GW}{m^2}$). Thus, making the suggested change to the β_0 parameter for helium improves the fit between the experimental value and model value.

In oxygen, the discrepancy between the model and experimenal values may be attributed to the experiments being conducted at different pressures. Their experiments were conducted at 450 Torr; the pressure in our prototype was not measured but the gases were fed into the system at 760 torr. The pressure in the chamber will affect the size of the plasma plume and the characteristics of micro-machined lines and structures. The plasma is smaller at high pressures and expands more at low pressures. Generally, the trend should show that the line

width in helium is highest and lowest in oxygen, but the experimental data demonstrates only a slight decrease in line width between helium and nitrogen with samples machined in oxygen having the highest line width.

Table 4.4: Comparison of the squared line width experimentally found in oxygen, nitrogen and helium with values determined using the regression-fit model by Lehr et. al (2014). Each experimental value is an average of 3 measurements using SEM at 26.1 $\frac{GW}{m^2}$. Each value has a unit of μm^2.

	Oxygen	**Nitrogen**	**Helium**
Model	2547.4	3445.1	6972.7
Experimental	9923.1	3259.8	3476.3

XPS Analysis

The first XPS analysis of samples machined in the prototype quantified the atomic composition of a polished and unpolished sample as shown in Table 4.5. The results for both samples were very similar; the three types of atoms present were titanium, nitrogen, oxygen, silicon and calcium. The atomic composition of the polished sample showed a high percentage of Si2p and $< 1\%$ of Ca2p. Strangely, the unpolished sample had a significantly lower composition of Si2p, and slightly higher compositions of Ca2p and N1s. The results demonstrated that the nitrogen composition was too low for samples micromachined in nitrogen and the polished samples contained silicon. The silicon was attributed to the sandpaper used to polish the samples before the experiments; the sonication was not effective in removing all the contaminants present on the surface. In a following experiment conducted with the same laser settings, the polished sample was sonicated for 10 minutes and wiped with acetone using a KimWipe® immediately before the experiments. In this case, silicon was only present in traces but nitrogen composition was still lower than expected for samples machined in a

nitrogen environment (*Wiped* in Table 4.5).

During the proof of concept experiments, the prototype chamber did not have the butterfly valve to control the flow of gas into the vacuum pump. So, after experiments were conducted, the vacuum pump was switched off and disconnected from the chamber before quickly covering the chamber port with a blank flange. This meant that the sample was exposed to the ambient environment for a few seconds which was enough for more reactive oxygen atoms in the air to react with the titanium surface. Flowing helium through the chamber after an experiment, but before exposure to ambient environment, yielded a higher N1s composition but the results were not consistent so adding a valve was a better solution (*He Flow* in Table 4.5).

Table 4.5: Atomic composition [%] of the polished, unpolished, wiped and helium flow samples.

	Polished	**Unpolished**	**Wiped**	**He Flow**
O1s	31.2	52.8	53.1	21.7
C1s	49.4	35.9	22.7	37.3
Ti2p	5.4	3.1	21.9	17.3
Si2p	10.7	5.0	0.8	0
Ca2p	1.9	1.8	0	0
N1s	0.7	1.5	1.5	23.7

4.2.3 Design & SOP Contributions

Figure 4.7 shows the key lessons learned from the proof-of-concept experiments. The line width analysis demonstrated that the design of the chamber will directly impact the physical surface characteristics. Replicating Lehr et. al.'s (2014) experiments would require a pres-

sure gauge added to the prototype chamber design. Moreover, the pressure of a system is known to affect the size of structures machined onto a metal surface (Lehr, 2015) so tuning surface topography in the designed chamber would require pressure control. While testing the prototype and developing an SOP does not require such an apparatus, this design shortcoming must be considered by future users of the finalized chamber. On the other hand, proper testing of the prototype must include complete protection of the samples during and after experiments before XPS analysis. Hence, a valve should be installed on the flange connecting the chamber to the vacuum pump. When experiments are completed, the valve on the gas line would be closed and the new valve on the vacuum line would also be closed. Doing this before disconnecting the gas and vacuum lines, and transporting the system to the glove box will prevent air from flowing into the system, thus preventing the contamination observed in the XPS results.

Further, future experimental methods should include a final wipe of the samples before loading into the chamber. After polishing and sonication, samples are typically stored in closed boxes but these don't prevent particles in the air from adsorbing onto the surfaces. As well, the XPS results show that particles from the sandpaper can also adsorb onto the sample surface so using a clean KimWipe with acetone will remove these contaminants.

4.3 Prototype Chamber Testing in Typical Experimental Conditions

A series of experiments similar to those found in literature (Kietzig et al., 2011; Bizi-Bandoki et al., 2013; Lehr et al., 2014) were conducted to determine whether the prototype chamber and current SOP were effective in protecting metal samples from air before analysis in the XPS apparatus. The prototype chamber was used to conduct the experiments since VTM custom-fitting was still under discussion with Thermo-Fisher Scientific.

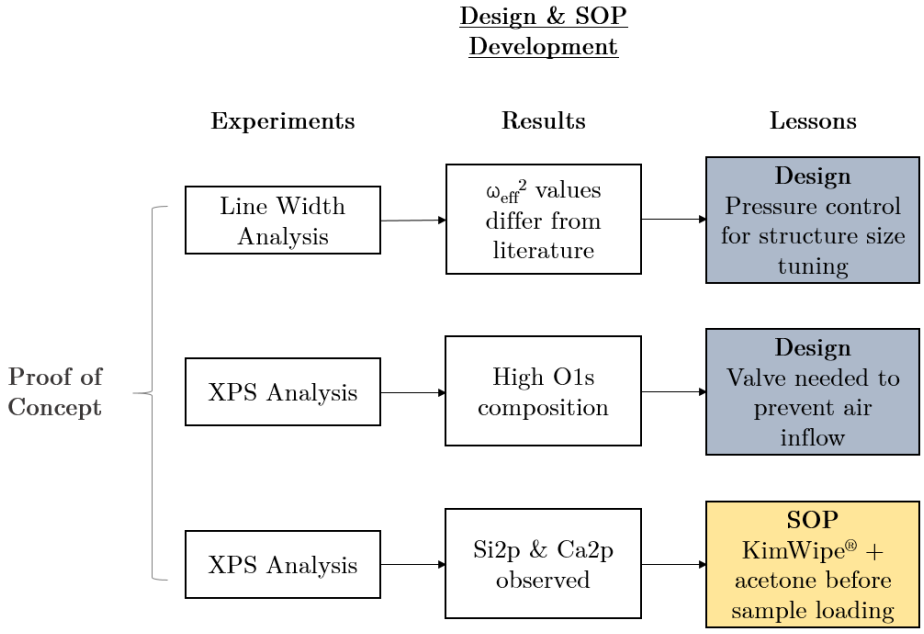

Figure 4.7: Summary of the contributions to chamber design and SOP from the proof-of-concept experiments.

4.3.1 Prototype Chamber for Gas & Vacuum Environment Experiments

Methods

To determine the strengths and limitations of the prototype for controlled environment experiments and inform the characteristics of a final chamber design, micromachining experiments were conducted in vacuum, nitrogen (Praxair, 99.9% purity) and helium (Praxair, 99.9% purity). Titanium (McMaster-Carr, 99.9% purity) sampleswere polished and sonicated in acetone for 10 minutes before experiments, and wiped with acetone using a KimWipe® immediately before experiments began. The samples were fixed onto the makeshift stage in the chamber and positioned co-axially to the left- and right-hand ports. Once loaded, the pump was run for 3 minutes to ensure that the chamber was under vacuum before micromachining took place. For experiments in gas environment, nitrogen or helium was fed into the system continuously. The positioning of the sample ensured that the gas flowed directly onto

its surface. Nanoripples were micro-machined on substrates using the following parameters (Table 4.6). Laser and scanning parameters for generating nanoripples were determined by trial and error.

Table 4.6: Laser and scanning parameters for generating nanoripple structures on titanium

Structure	**Power (mW)**	**Scan speed (mm/s)**
Nanoripples	20	1.5

Following laser micromachining, the gas and vacuum lines were closed shut before the pump was switched off. After disconnecting the lines, the chamber was un-fastened from the stage and transferred to the glove box, where the sample was unloaded and placed into the VTM. The VTM was evacuated in the glove box transfer port before loading into the XPS apparatus (Thermo Fisher Scientific, K-Alpha). XPS analysis consisted of a general survey to understand the surface composition of the sample and SEM was used to observe the surface topography. SEM imaging was conducted after XPS analysis. To quantify the difference in atomic composition of samples processed in a controlled environment, control samples were micromachined under the same conditions and exposed to the ambient environment following micromachining. The controls were analysed via XPS following exposure to the environment.

Results

Using the Chamber & SOP

During these experiments, a few observations were made regarding the chamber and SOP designs. Each experiment consisted of one patch machined on a titanium sample under the specific gas conditions (Vacuum, He or N_2) before transfer in the glove box to the VTM. Three repetitions were conducted for each gas condition, so after a sample was unloaded into the VTM in the glove box, the chamber was returned to the 3D stage for the next

experiment. This also implies that the sample was stored in the glove box until all the repetitions were completed before the VTM was evacuated for transport to the XPS. The time required to load a sample into the chamber, machine a patch, load the chamber into the glove box, unload the sample into the VTM and return the chamber to the 3D stage was about 30 minutes. This meant that 3 repetitions would take about 2 hours, exclusive of the time required for XPS analysis.

The machining process was generally straightforward to implement, however minor misalignments in the positioning of the sample in relation to the lens would result in patches not being machined or misshapen patches. Since the experiments cannot be viewed in real-time, the errors would only be found when the sample was unloaded into the VTM. Experiments in O_2 were not suitable for the glove box environment, where the oxygen concentration is maintained at <1 ppm.

Surface Topography & Nanoparticle Accumulation

The samples were not sonicated after machining to determine whether the pump was effective at removing the nano-particles. The first observation is that having continuous gas flow over the sample is effective at preventing accumulation of nano-particles. The surface topography is completely visible after laser micromachining as seen in Figure 4.8. The nano-ripples settings were effective in nitrogen and vacuum environment. In helium, the settings generated structures similar to bumps suggesting that the gas environment influenced the observed topography.

Surface Chemistry

XPS data denotes the amount of one atom relative to other atoms present. C, N, Ti and O were present on almost all the samples except the He-VTM samples. According to Figure 4.9, Ti2p composition did not vary greatly among the samples. O1s composition remained about the same on both samples exposed to air (Vac-Air, He-Air) and those transferred via VTM (Vac-VTM, He-VTM). However, the reduction in O1s atoms between N_2-Air and

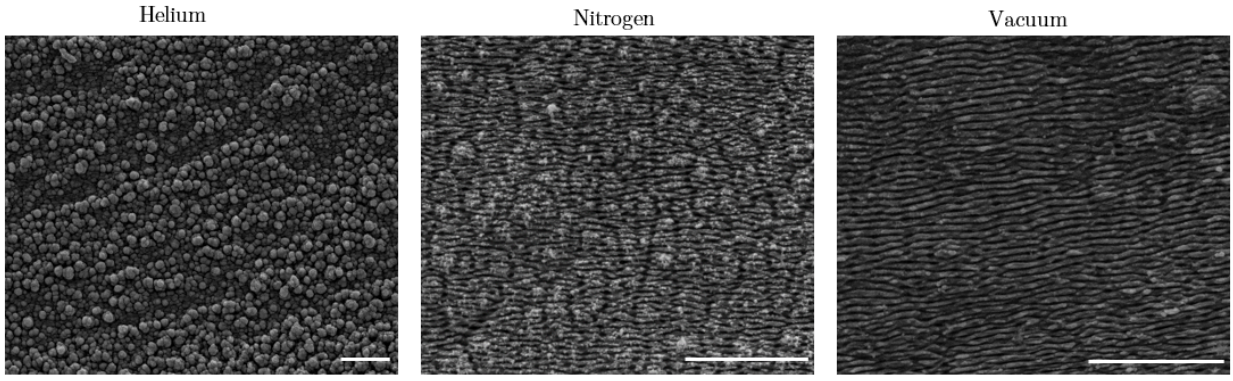

Figure 4.8: SEM images illustrating the surface topography of samples machined in He, N_2 and vacuum environment. All length scales are 10 μm.

N_2-VTM samples was over 10%, which might be attributed to the over two-fold increase in N1s atoms. As well, all the samples transferred via VTM (Vac-VTM, N_2-VTM, He-VTM) had less C1s atoms but the reduction was most pronouced between N_2-Air and N_2-VTM samples. Vac-VTM samples were not completely devoid of N1s atoms unlike the He-VTM samples.

Discussion

Design Effectiveness

The prototype chamber was effective in protecting the samples surfaces from the ambient environment as proven by the lower C1s atomic composition after transfer to the VTM (Vac-VTM, N_2-VTM and He-VTM) and lower N1s composition on He-VTM and Vac-VTM samples. Further, the increased N1s composition and absence thereof on N_2-VTM and He-VTM samples respectively implies that the chamber is also effective in delivering a uniform gas environment. The presence of N1s on the Vac-VTM surfaces may indicate adsorption on N_2 molecules from the glove box environment.

Chamber Limitations & Impacts

- The time cost associated with machining one sample and transferring it to the VTM

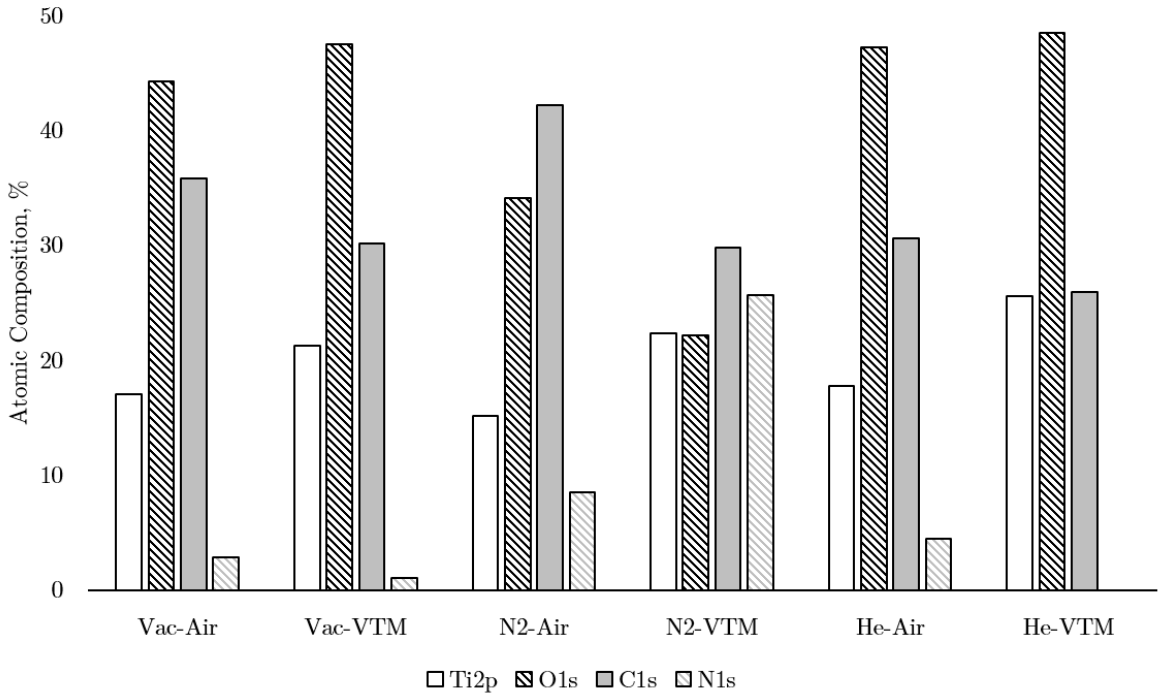

Figure 4.9: Atomic composition of the samples prepared in the prototype chamber and transferred through a glove box to the VTM for surface chemsitry analysis in the XPS apparatus

is high at 30 minutes. A chamber with the capability of machining multiple samples under the same gas conditions would greatly reduce the time spent.

- As well, the ability to monitor experiments in real-time would prevent mishaps and allow the user to immediately rectify minor misalignments. Adding a window might be a solution to this problem.

- Without flow rate or pressure information it is difficult to pinpoint why for instance, nano-ripples were generated in vacuum and nitrogen but the same settings yielded bumps in helium.

Lessons for SOP Development

- The user must always check that the VTM is under vacuum by evacuating it in the transfer port, loading it into the glove box and turning it upside down to check if

the cap opens. Doing this before removing the VTM from the glove box will ensure that samples are not exposed to the environment in the event that the VTM did not evacuate properly.

- Misalignments between the sample and the lens can be avoided by ensuring that the makeshift stage is loaded into the chamber in the exact same position for each experiment.

4.3.2 Impact of Varying Laser & Scanning Parameters

Based on the observation that bumps, instead of nano-ripples, were generated in helium during the previous experiments we ventured into testing other laser settings to observe whether the predicted topography was generated. The chosen laser parameters will test the limits of the chamber with regards to incident laser power and nanopaticle accumulation. The results will show whether the design is sufficient for experiments at extreme laser parameters. In addition, the link between surface topography and surface chemistry of laser micro-machined metals will be highlighted to corroborate findings in literature (Lehr et al., 2014).

Methods

Two sets of parameters (Table 4.7) were chosen to generate *aggregate* and *chaotic* structures based on literature (Biswas et al., 2016). The laser and scanning settings were used to machine titanium (McMaster-Carr, 99.9% purity) samples prepared using the same techniques in earlier testing experiments. The updated SOP (Figure 4.10) was implemented during these experiments but the prototype chamber was not modified in any way. The machining experiments were conducted in nitrogen and vacuum environment. XPS was used to determine the atomic composition of the sufaces post-machining using an X-ray spot size of 400μm. After XPS analysis, the samples were sonicated for 10 minutes to reveal the generated structures through SEM imaging.

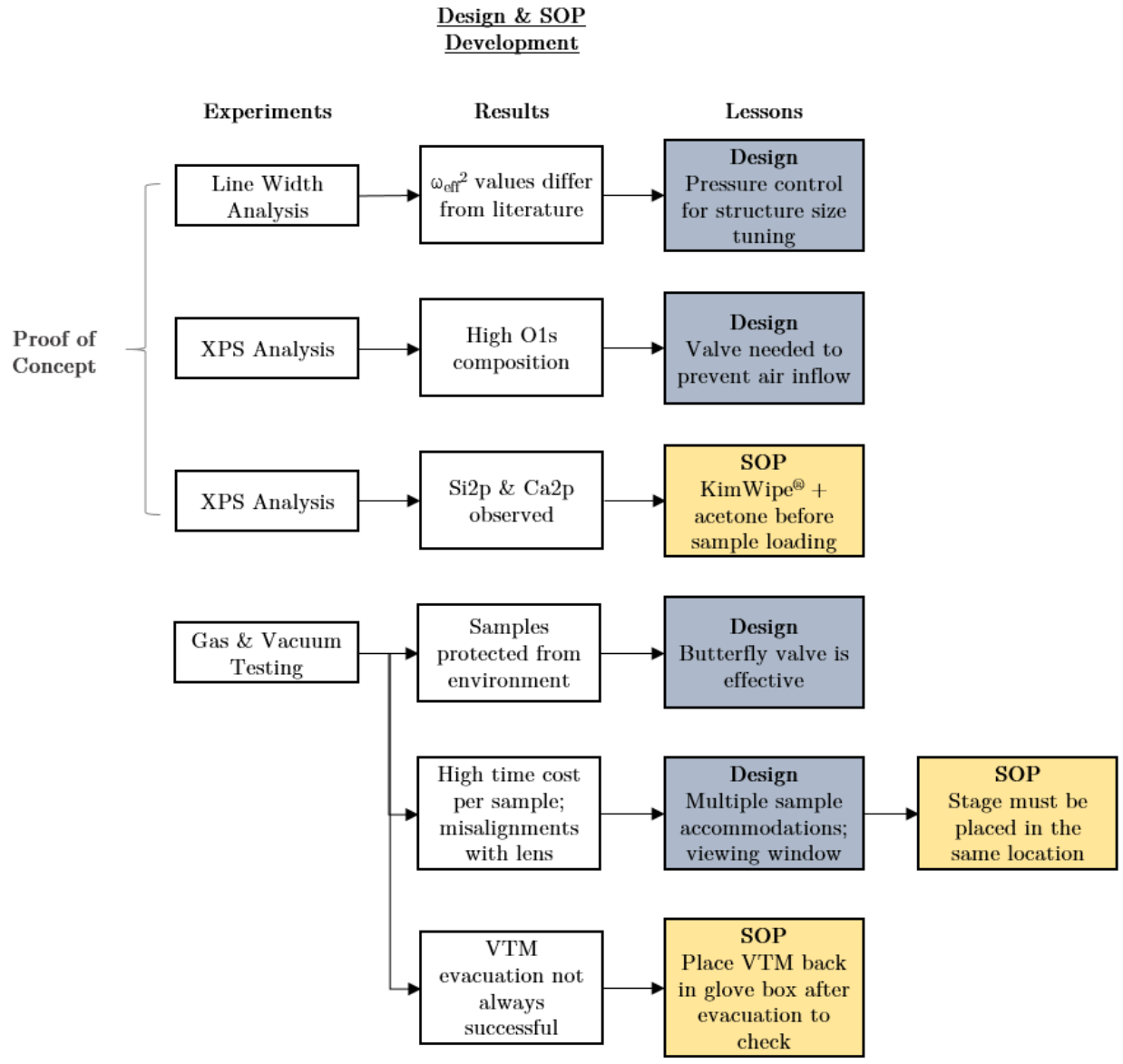

Figure 4.10: Summary of the contributions to the design and SOP development from the chamber testing for gas and vacuum environments

Results

Using the chamber & SOP

At the low speed of 0.1 mm/s required for *aggregate* structures, nanoparticle accumulation was observed on the chamber window after each experiment. The dark grey nanoparticles agglomerated on the chamber window and would at times prevent the laser beam from

Table 4.7: Laser and scanning parameters for generating aggregate and chaotic structures on titanium

Structure	**Power (mW)**	**Scan speed (mm/s)**
Aggregates	12	0.1
Chaotic	150	1

traveling through the window to the sample. Also, nanoparticle dust was noticed inside the chamber after experiments. To prevent accumulation, the window and interior of the chamber were cleaned with ethanol after each experiment. The high power necessary for *chaotic* structures did not immediately affect the chamber window. The chamber window began to darken or brown after 3 experiments, as a result the window had to be re-positioned after each experiment to prevent hindrances to the laser beam travel.

Again, the limited space between the lens and the chamber window meant that it was impossible to view a sample once it was loaded into the chamber, hence troubleshooting machining errors and manipulating samples were impossible tasks once the chamber was fastened to the stage. The vacuum pump was connected to the prototype chamber with rigid steel tubing that restricted the motion of the stage when in use. When connected to their respective lines, the left and right ports of the prototype chamber make the chamber unbalanced. Thus, when the chamber is experiencing too much force from the vacuum pump or too tightly fastened to the stage, the stage will become unbalanced and begin to whine. This issue was typically rectified by re-positioning the chamber or the vacuum line.

Surface Topography

Figure 4.11 shows that neither of the settings for *aggregate* and *chaotic* structures generated the desired topography in both vacuum and nitrogen environments according to literature (Biswas et al., 2016). Furthermore, the generated structures differ greatly between

Table 4.8: A summary of the structures generated in nitrogen and vacuum environments using the laser settings known for creating *aggregate* and *chaotic* structures

	Nitrogen	**Vacuum**
Aggregate	Bumps	Undulating grooves
Chaotic	Ripply bumps	Cones

the environments. In nitrogen, the *aggregate* structures look like bumpy structures decorated with nanoripples. On the other hand, the same laser and scanning parameters yield undulating grooves in vacuum. In vacuum, the predominant structures are more ordered and of a shorter length scale than the nitrogen-processed samples. The *chaotic* structures generated in nitrogen appear to be transitioning from nano-ripples to bumpy structures. In vacuum, the structures appear *cone-like* with nano-ripple decoration. Table 4.8 summarises the actual structures generated at the laser and scanning parameters.

Surface Chemistry

The chemical composition of the bumpy (bumps and ripply bumps) structures machined in nitrogen are almost equivalent. Ti, O, C and N were present on both structures within a range of 5%. In vacuum, there was no nitrogen detected on the undulating grooves and cones but the atomic compositions differs significantly between the two structures with respect to the Ti, O and C. The undulating grooves contain half the Ti2p atoms and double the C1s atoms when compared to the cone structures. The O1s content of the cone structures is almost 20% more than the undulating grooves.

Discussion

Design Effectiveness

It was expected that the gas environment would affect the types of structures generated at given laser and scanning parameters. This is because the background medium changes

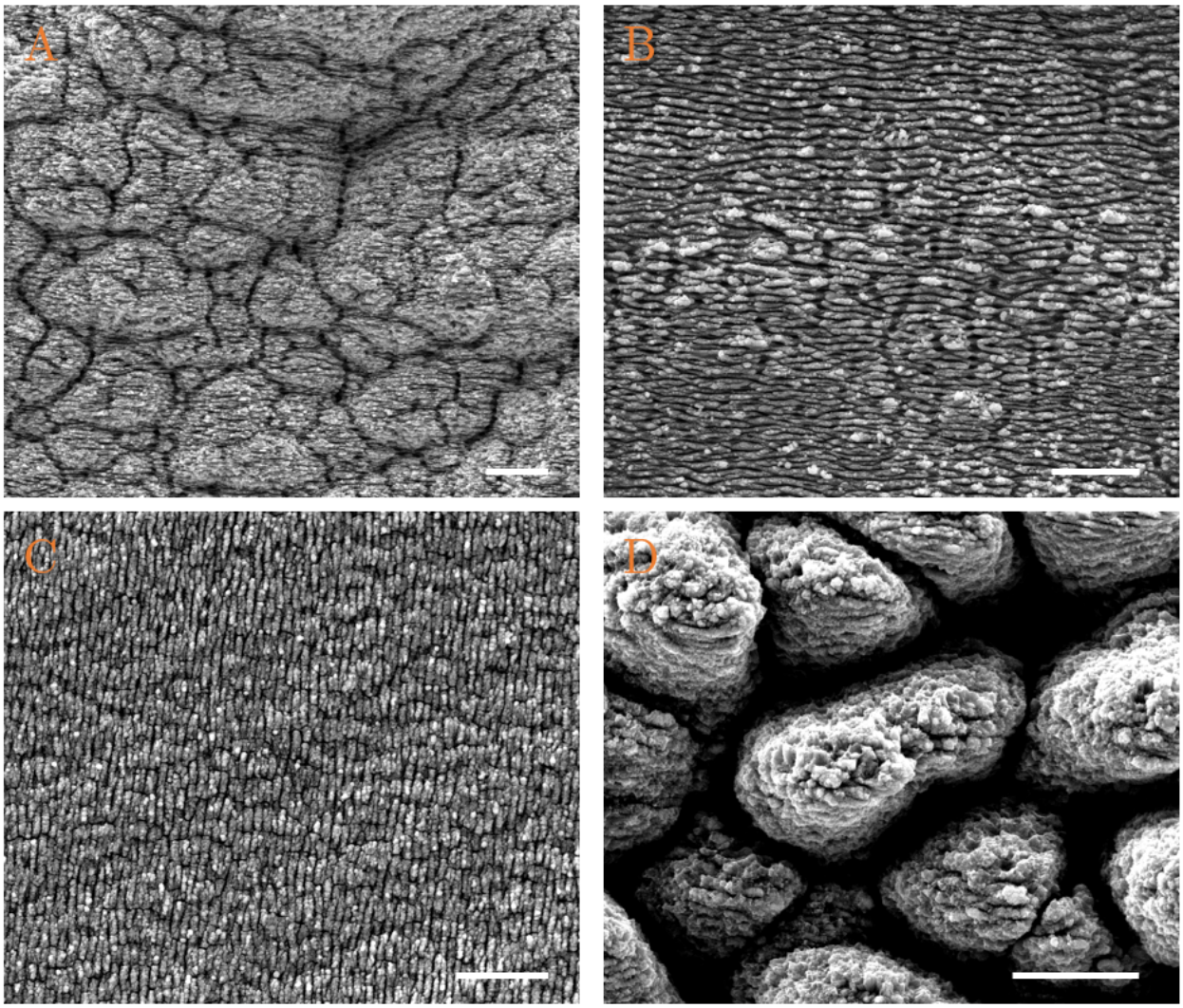

Figure 4.11: SEM images illustrating A-Bumps; B-Undulating grooves; C-Ripply Bumps and D-Cones machined in N_2 (top row) and vacuum (bottom row) environment using settings for *aggregate* and *chaotic structures*. All length scales correspond to 5 μm.

the properties of the plasma generated at the ablation interface. Thus, the nano-ripples generated in helium varied from those made in nitrogen as shown in the Chapter 4.3.1. The effect is more pronounced when coupled with changes in pressure. As such, the bumps and ripply bumps generated in nitrogen were transformed to undulating grooves and cones, respectively, in vacuum. The chamber and updated SOP were effective in protecting the samples from the ambient environment. All the samples machined in vacuum did not have

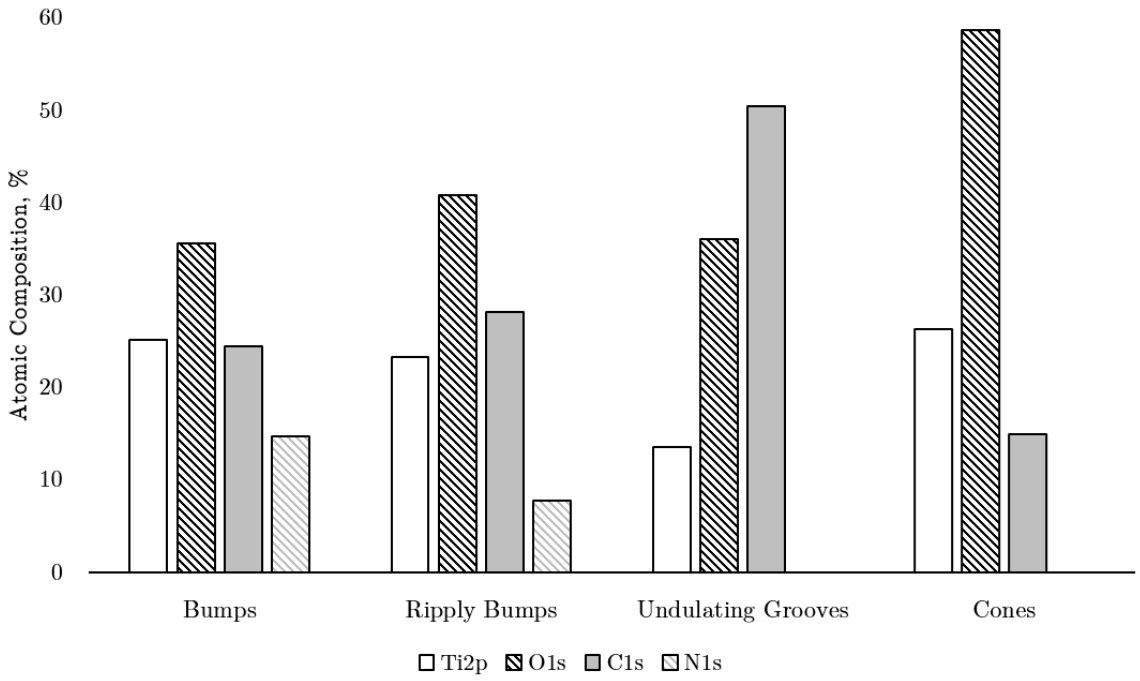

Figure 4.12: Atomic composition of the samples micromachined with *aggregate* and *chaotic* structures in nitrogen and vacuum environments

nitrogen atoms on their surfaces.

Chamber Limitations & Impact

- Kodial glass window was not effective at high power and began to brown. As prescribed by Museur et. al. (Michel et al., 2007), the window should be replaced with a sapphire glass window and monitored for discolouration.

- At very low speeds where nanoparticle generation is high, the gas flow is not sufficient to prevent accumulation on the window. A compact method of nanoparticle removal is necessary to ensure that the laser beam will be able to reach the sample without encountering a foggy window.

- The 3D-axis stage's balance is sensitive to minor position changes to the chamber. A chamber with a lower center of gravity and a vacuum line that is less rigid would

alleviate this problem.

Lessons for SOP Development

- Nanoparticles that accumulated on the window and in the chamber were removed with ethanol. Attempts to clean the surfaces were made with acetone but the nanoparticles became filmy.

- The results corroborated that topography is related to surface chemistry. For structures like the cones with accentuated nano-clustered peaks and deep trenches, an X-ray spot size of 400 μm may not be effective in registering the varying surface composition. Thus, future operators who are concerned with micro- or nano-scale chemistry should adjust the spot size accordingly.

4.4 Chamber Design Choice & Finalized SOP

Recommendations were made to the future operators of the chamber based on the experimental findings on the design and updated SOP (Figure 4.13). They clarified that flow or pressure control and the ability to view the experiments were not necessary to their planned experiments, but the design should be robust enough to accomodate the necessary apparatuses in the future. Nanoparticle accumulation can be easily rectified by cleaning the chamber and window intermittently so it was also not a pressing concern. Finally, multiple samples should be accomodated in the final design and the window must be replaced with higher quality sapphire glass to prevent browning. With regards to the SOP, the recommendations were not problematic and the make-shift stage positioning would be rectified in the final chamber design.

Thus, in addition to the criteria listed in Chapter 4.1.2, sample loading time, sample accomodation and chamber mounting of the design options were evaluated (Table 4.9). The costs were also updated to include the price of sapphire glass.

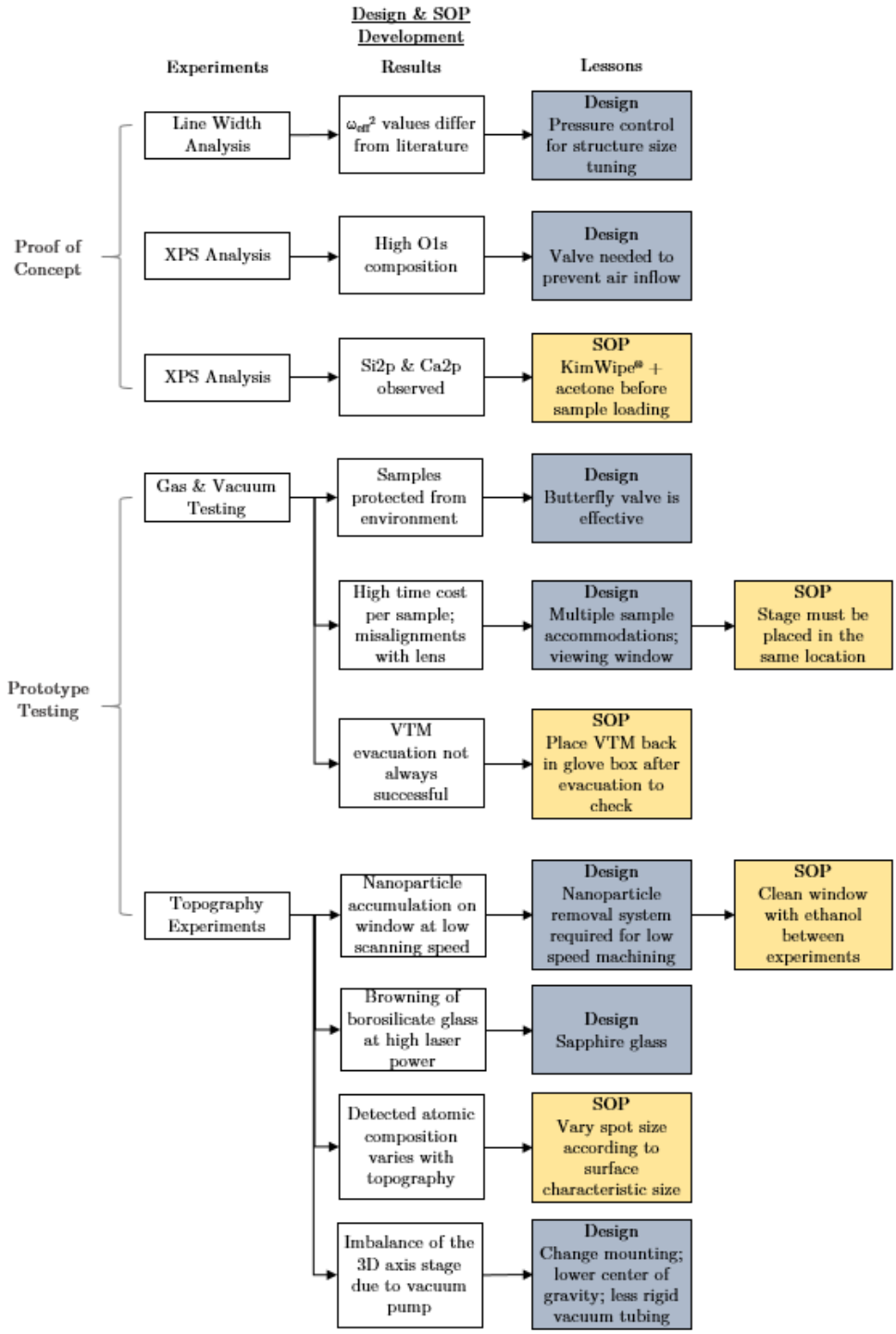

Figure 4.13: The chamber design and SOP development flow chart was updated to reflect the findings of the topography experiments

Table 4.9: Summary of each chamber option and its characteristics after prototype testing

	4-way Cross	**5-way Cross**	**Cube**	**VTM**
Cost	$541	$1032	$2820	$12000
Sample loading time	10 min	10 min	2.5 min	2.5 min
Weight	1.3 kg	1.3 kg	3.0 kg	0.6 kg
Height	70 mm	50 mm	94 mm	40 mm
Width	100 mm	80 mm	94 mm	91 mm
No. of samples	1	1	4	4
Mount	screw	posts	holder	none

4.4.1 Re-evaluation of Design Options

4-way Cross

Advantages

- The 4-way cross is available and has already been modified for the prototype testing.

Disadvantages

- Inner diameter of the flange is too small to accommodate a wider sample holder that can carry more than one sample.
- In the future, adding more accessories to the chamber would be virtually impossible since all the ports are already in use. Using a tee flange would compound the balance issues.
- The mounting method with the screw affects the balance of the 3-D stage, continuing with this mounting method may result in damage to the 3-D stage. A different mounting method is difficult to implement because of the clamps around the bottom flange and the high center of gravity of the system.

- Sapphire glass is not available in KF-25 flange size from both Kurt J Lesker and MDC Vacuum Products. The window would have to be custom-made.

5-way Cross

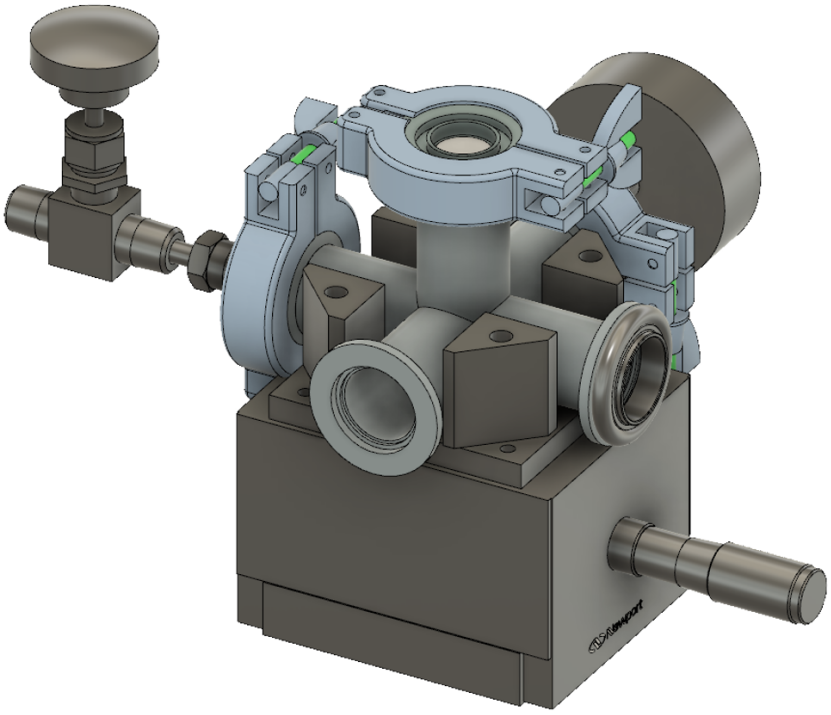

Figure 4.14: A CAD image of the 5-way cross affixed to the 3D stage with posts at each corner to secure the chamber.

Advantages

- Low centre of gravity would improve balance since four of the chamber ports would sit directly on the stage. The chamber could be mounted with four posts each located between the flanges.
- The two extra ports could be used in future experiments for more accessories (viewing window and pressure control).
- Sapphire glass window available.

Disadvantages

- Only one sample can be loaded into the system so the processing time would be high.
- The two extra ports may hinder glove box transfer when valves are attached to the system.

Cube

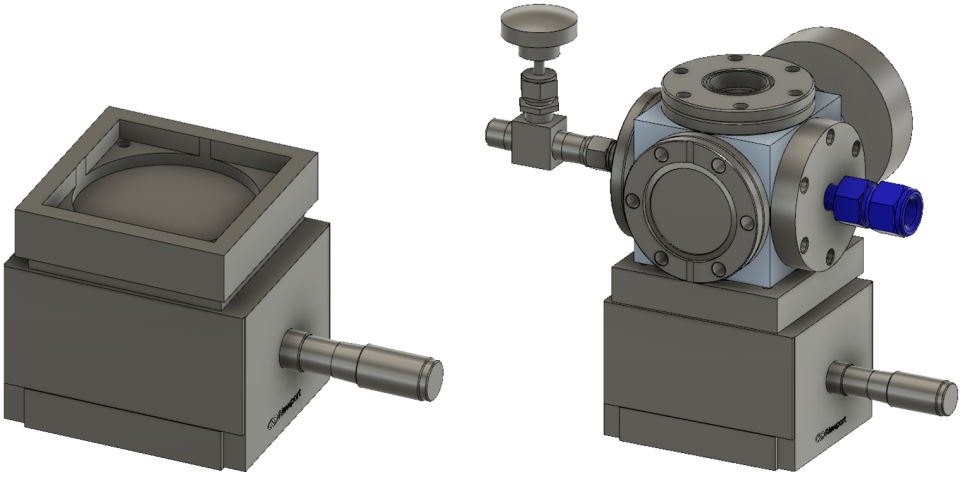

Figure 4.15: A CAD image of the cube affixed to the 3D stage with a 3D printed holder (left). The CAD of the holder is on the right.

Advantages

- Compact design with ports tightly wrapped around the body, making it the most balanced option. The chamber would be mounted using a lightweight 3-D printed holder that is screwed to the stage.
- The sunken edges of the 3-D printed holder will be used to align the chamber and its components with the laser beam.
- Sapphire glass window available.
- The interior of the cube and the flange size are wide at 70 mm width, so more samples can be loaded into the system for machining.

- Two extra ports would be useful for further customization (pressure gauge and viewing window).

Disadvantages

- Most expensive home-made option.
- The cube is also the heaviest option before accessories.

Custom-fitted VTM

Advantages

- The VTM already has space for four samples.
- The VTM has a flat base so it would sit directly on the stage with no need for fastening or mounting. It is also the shortest option, so samples can easily be monitored during experiments.
- Once under vacuum, the samples can be machined and transported to the XPS apparatus, thus skipping the glove box chamber entirely.

Disadvantages

- There would be little space between the sample and glass window, which may hinder nanoparticles from flowing out of the system.
- Pressure control of the system would be impossible since there are no ports to attach a pressure gauge.
- The interior of the cube and the flange size are wide at 70 mm width, so more samples can be loaded into the system for machining.
- The cost estimate of a custom-fitted VTM was about $12,000, making it the most expensive option.

The VTM was disqualified as an option after discussions with the manufacturer proved fruitless; designs and detailed quotes were not provided. Of the three home-made chamber options, the cube is the most suitable and robust option because it can house more samples, it poses the least risk to the 3-D stage balance and can be modified in the future with more accessories.

4.4.2 Design Considerations for the Cube

The chamber weighs 1.2 kg, making it significantly heavier than the prototype so the accessories must be light or must be added to the setup at locations that are far from the stage. The sapphire window (Kurt J Lesker, VPZL-275SW) weighs 0.25 kg and the CF flanges (Kurt J Lesker, F0275X000NT) each weigh 0.34 kg; the chamber will require a maximum of 3 CF flanges. The gas line will have a CF flange with a swagelok connection (Kurt J Lesker, F0275X4SWG) that pairs with the ball valve (0.15 kg) used in the prototype. Instead of using a butterfly valve directly on the chamber port, a CF flange with a 1/4" swagelok connection will pair with a plastic tube with a stainless steel mesh protective wrap (Swagelok, SS-CT8PM8PM8-12). The tube will lead the gas flow out of the chamber about 0.3 m away before connecting to the butterfly valve which will control the flow of air or gas to the vacuum pump. The tube improves the weight distribution on the 3-D axis stage and reduces the *pull* of the vacuum pump on the chamber when switched on. Each swagelok-fitted CF flange weighs 0.28 kg, thus the cube chamber with accessories weighs 3.03 kg. Since the maximum weight carried by the 3-D axis stage is 3.8 kg, extra parts or accessories attached to the chamber must weigh less than 0.8 kg.

The 3-D translation stage comprises of expensive equipment totalling over $20,000 that are integral to all laser micro-machining experiments in the BSEL group. In fact, the stages were recently upgraded with $7,000 worth of modifications to facilitate 5-D range of movement. The high cost is a direct result of the high precision of stages; in particular, the x- and

y-axis stages each have an accuracy of ±0.2 μm and bi-directional repeatability of ±0.030 μm. When an imbalance is sensed in the system, the stages try to maintain precision, which is why the whine is heard. Due to the desired precision and required compatibility with the external stage controller, replacing the stages to improve weight distribution of the chamber was not a reasonable option for the final design. Nonetheless, during the installation of the recent modifications, it was discovered that there are two parameters (scaling acceleration and acceleration limit) which control the acceleration of the x- and y-axis stages and both depend on the weight applied to the stages. Therefore, the parameters should be updated for any increase or decrease in weight in order to achieve maximum acceleration. As well, the PID controller for the stages should be tuned to prevent the 'whine' heard during some of the chamber testing experiments. An SOP for taking these actions were prepared by a previous student for the BSEL group.

The sapphire window attached to the cube chamber has a refractive index of 1.77, a thickness of 2 mm, transmits light with wavelengths between 250 nm to 3750 nm (UV to IR range) and will be placed directly below (4 mm away) the 100 mm lens. Using the beam extension formula outlined earlier (Equation 2.3), the theoretical beam diameter after the window is 41 μm.

The major drawback of the prototype chamber was the inability to micromachine multiple samples in one session. The cube chamber has a minimum width of 70 mm internally, providing enough space for a sample holder that can carry up to 4 samples. Initially, we considered a holder connected to a servo motor with capability of 360° rotation as shown in Figure 4.16. The motor would be controlled by an Arduino UNO; the two would be connected with three wires (ground, 5 V and signal) that thread through a modified CF flange. The CF flange has 4 copper conductors that connect wiring fom inside to outside without affecting the seal of the chamber. The stage would have been placed such that the sample is directly in the path of the laser beam, after micromachining a sample, the Arduino

switches the motor on and sends a signal for 90° rotation. When the sample holder rotates, the next sample moves into the laser beam's path for micromachining. This design was not pursued further because servo motors do not rotate precisely. Specifically, at each turn, the servo motor would rotate between 80° and 100° meaning the sample would not always be in the beam path.

Knowing this, a new design that did not require electrical or mechnical parts was formulated: a simple sample holder consisting of a stand with four marked locations for samples (Figure 4.17). Samples must have the same thickness to ensure that each experiment is conducted at focus. The holder will be secured to the centre of the bottom flange with two L-clamps, such that the holder is completely visible through the chamber window from the top. The L-clamps will be fabricated from aluminum and welded to the bottom flange such that the sample holder is restored to the same position during loading. Once the chamber is loaded onto the 3-D stage, the operator can move the stage and chamber to the coordinates that place the sample in the beam path. The instructions on loading and unloading samples onto the holder, programming a machining trajectory and maximum sample dimensions can be found in the Appendices.

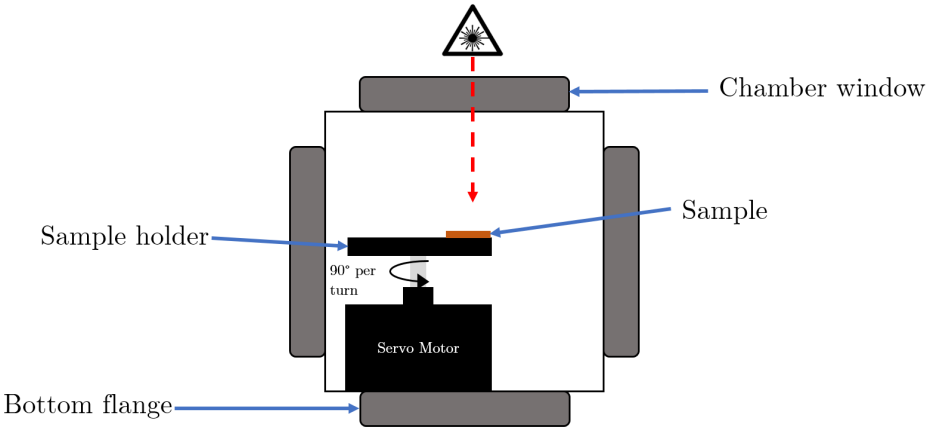

Figure 4.16: A diagram of the electronic sample holder consisting of a servo motor in the cube chamber.

A future consideration is the lack of precision in gas flow between experiments because

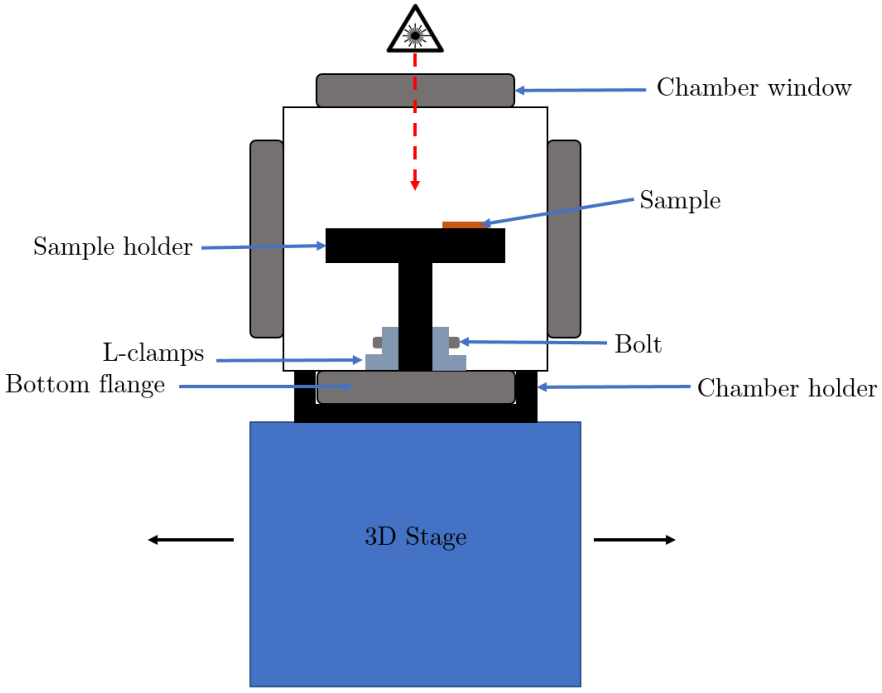

Figure 4.17: A diagram of the simple sample holder in the cube chamber. The 3D stage will be used to move the sample into the beam path.

there was no flow meter. Yet, the high cost of mass flow meters made them an unsuitable option at this stage of the design and assembly process. Mass flow meters cost upwards of $2000 and require precise calibration for the specific gas to be used in experiments. Nonetheless, such an accessory can be added to the design when appropriate. As well, rotameters are less expensive devices for flow measurement and would only require a union tee swagelok connection, in order to be attached to the gas line. In the event that pressure in the chamber is a useful parameter, one of the two blank CF flanges can be modified to include a pressure gauge that is within the weight limitations of the 3-D axis stage.

The updated SOP for the prototype chamber and cube chamber can be found in the Appendices.

Chapter 5: Nanoparticle Collection

During the prototype testing discussed in Chapter 4.3, it became clear that conducting experiments with gas flowing directly above a sample is not always sufficient in preventing nanoparticle accumulation for all laser parameters. When generating nanoripples in Chapter 4.3.1, excessive nanoparticle accumulation was not observed but at low scanning velocities in Chapter 4.3.2, nanoparticle accumulation was observed in the prototype chamber, on the window and on the samples. Hence, there is a need for an additional method for nanoparticle removal that is compatible with a closed environment setup.

The proposed nanoparticle removal method is based on the theory that nanoparticles have a surface charge. A series of experiments were conducted to explore whether a charged titanium or copper sheet can attract or repel nanoparticles generated during a micromachining experiment. Figure 5.1 summarizes the experiments that were conducted and the major findings; it will serve as a visual guide for this chapter.

5.1 Proof of Concept Tests

Ripples were micro-machined on copper and titanium samples (99% purity, McMaster-Carr, USA) with a laser beam with wavelength of 800 nm, repetition rate of 1 kHz, and pulse duration of ∼150 fs. Ripple structures were chosen because the laser parameters are experimentally known to generate a large amount nanoparticles due to the high power and low scanning speed. Titanium and copper samples were cut to rectangular sheets measuring 1”

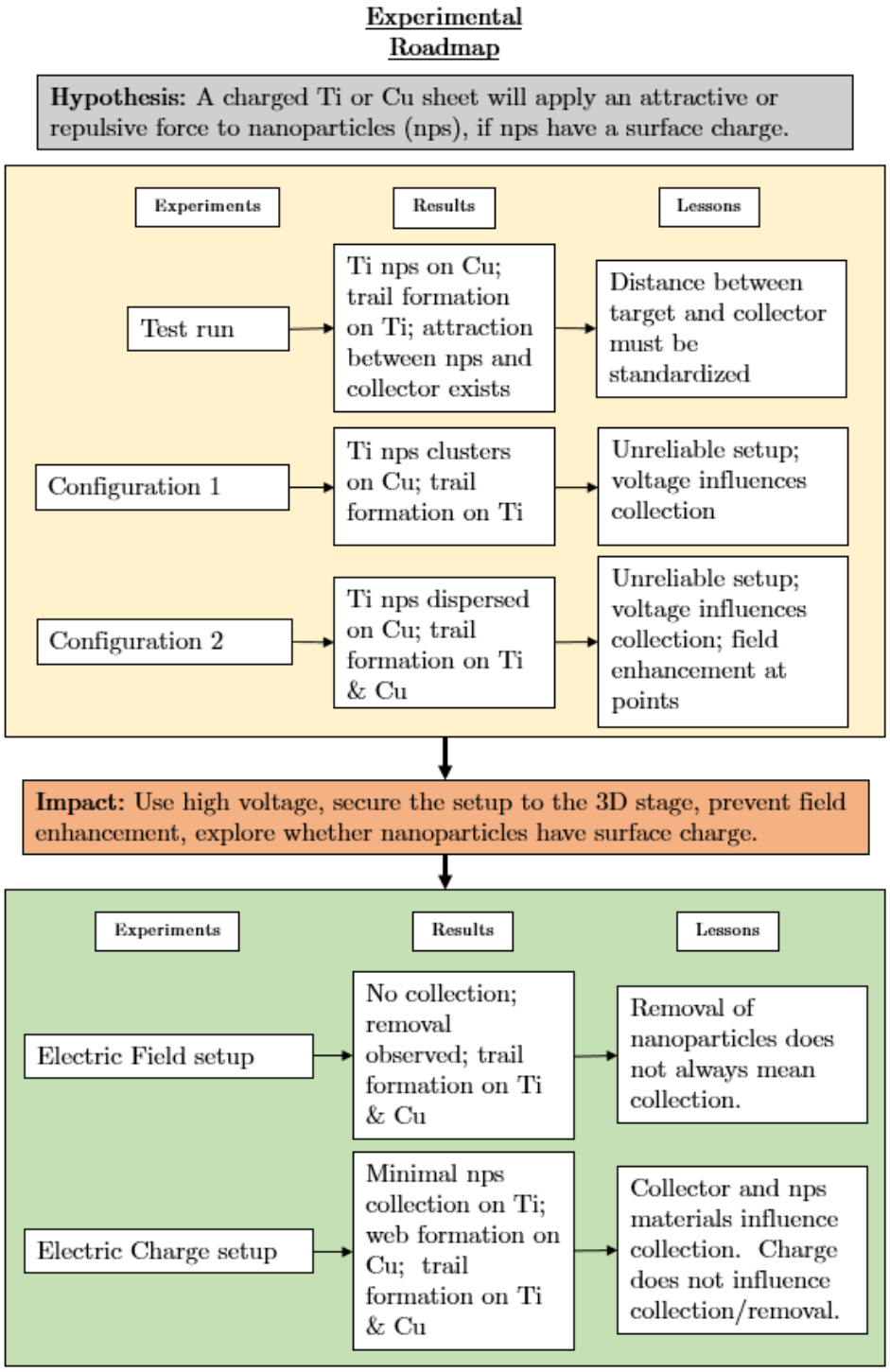

Figure 5.1: The experiments conducted are summarised in the flow chart. In the yellow box are the proof-of-concept experiments which informed the plan of actual experiments in green.

by 0.5"; circular copper samples with 0.5" diameter were later used in experiments. There are two types of samples in the following experiments: the target samples which were ablated and the collector samples which were used to attract nanoparticles generated during ablation. Both sets of samples were imaged using SEM.

5.1.1 Test Run

The first challenge was to answer the following questions:

- Do nanoparticles have a surface charge?
- Are they positively or negatively charged?
- If there is a charge, can it be used to transport nanoparticles from an ablated surface to a collector sample?

Basic experiments were conducted using titanium sheets as target samples and copper sheets as collectors. The titanium samples were fixed to the stage using double sided tape and the copper collector samples were L-clamped to the stage beside the target. In each trial, three patches were micromachined consecutively on the target sample while the collector sample was connected to a power supply operating at 100 V. SEM images of the target and collector samples were taken; the results are summarised in Table 5.1.

Table 5.1: A summary of the trial runs completed at 100 V with varying polarity.

	Target Polarity (Ti)	**Collector Polarity(Cu)**	**Collected nps**
Trial 1	none	-	minimal
Trial 2	none	+	yes
Trial 3	-	+	no

In Trial 1 some nanoparticles were collected on the copper sheet (Figure 5.2) but Trial 2 was more successful with the thick web of nanoparticles collected on the copper surface

(Figure 5.3). Trial 3 was not successful as there were no nanoparticles visible on the copper collector (Figure 5.4).

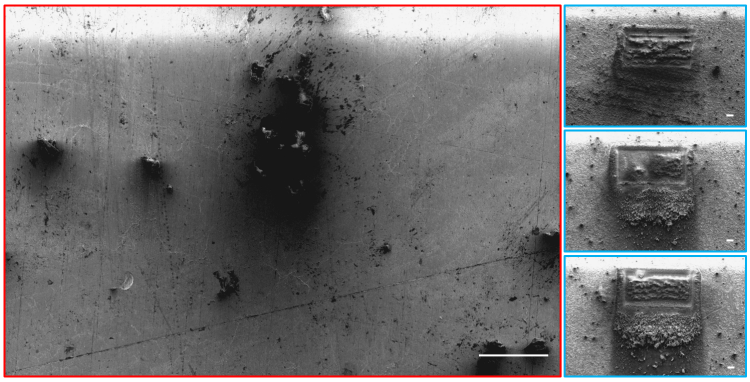

Figure 5.2: Trial 1: SEM images of the copper collector (left, red) and the three patches machined consecutively on titanium (right, blue) at -100V. Scales correspond to 100 μm.

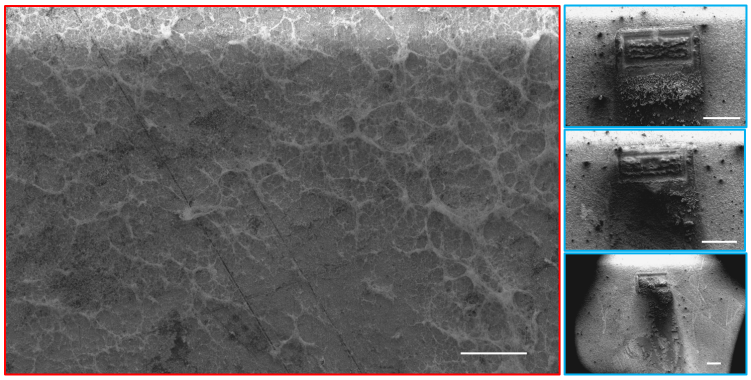

Figure 5.3: Trial 2: SEM images of the copper collector (left, red) and the three patches machined consecutively on titanium (right, blue) at +100V. Scale is 200 μm (left) and 500 μm (right).

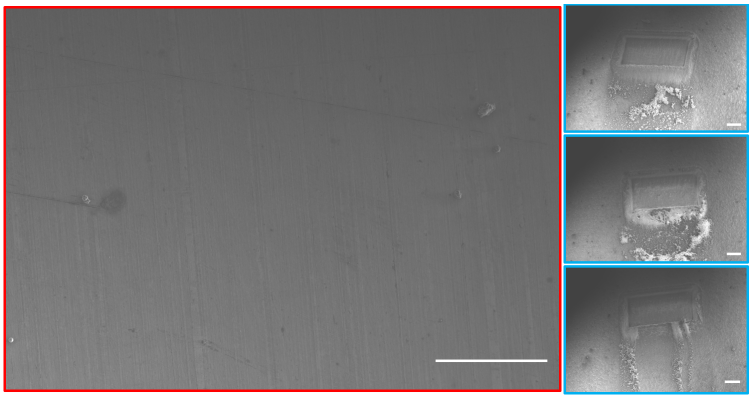

Figure 5.4: Trial 3: SEM images of the copper collector (left, red) at +100 V and three patches consecutively machined on titanium (right, blue) at -100V. Scale is 100 μm (left) and 200 μm (right).

The first trial tests appear to show that titanium nanoparticles have a negative surface charge as they are mainly attracted to the positively charged copper collectors. Nonetheless, the minimal collection of nanoparticles on the negatively charged collectors suggests that there was an interaction between the nanoparticles and the collector. Since the distance between the collector and target samples was not measured or controlled, the next series of experiments were focused on adding about 1 inch of space between the samples and testing two configurations. Further, we aimed to determine whether material choice of the target and collector samples would influence collection.

5.1.2 Configuration 1

In the first configuration, the target and collector samples were taped to a 3-D printed sample holder at a 90° angle to each other (Figure 5.5). The distance between the machining area and the collector sample was maintained at about 1 inch.

Table 5.2: A summary of the results from the experiments using Configuration 1.

Target/Collector Pair	**Collector Voltage(Cu)**	**Collected nps**
Ti/Cu	+500 V	no
Ti/Cu	-500 V	no
Ti/Cu	+100 V	no
Ti/Cu	-100 V	no
Cu/Ti	+500 V	no
Cu/Cu	-500 V	no
Cu/Ti	+100 V	no
Cu/Cu	-100 V	no

Experiments with this configuration were difficult to complete because the setup was

unreliable. The sample holder was fixed to the 3-D translation stage using double-sided tape. During experiments, the collector would either loosen from the holder or the entire holder would detach from the 3-D translation stage. At +100 V and -100 V with copper collectors and titanium machined samples, the setup remained intact and SEM images of the collector sample (copper) showed clusters of titanium on the surface (Figure 5.6).

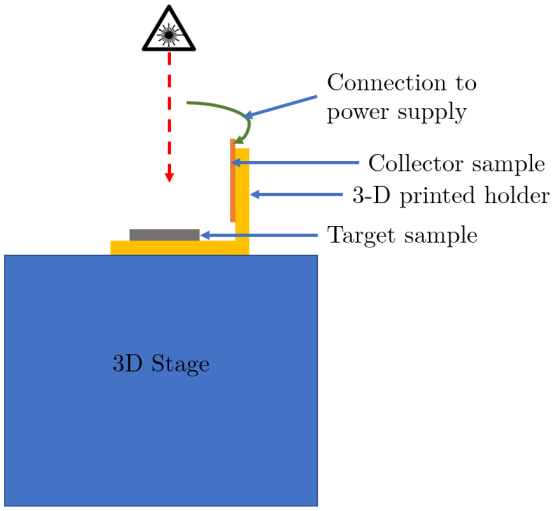

Figure 5.5: A schematic diagram of Configuration 1.

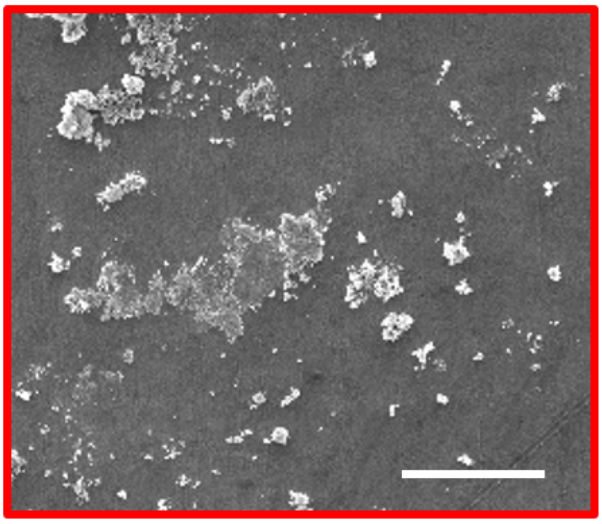

Figure 5.6: SEM image of the copper collector titanium nanoparticle clusters found on copper collector.

In the other experiments, the setup was disrupted and the SEM images showed no nanoparticles on the collectors. Further, the clusters of titanium nanoparticles collected

at +100 V and -100 V are not accepted to be a result of the voltage or charge on the collector sample, since it is unlikely that the particles would be transported in such a high concentration and agglomerate on the surface. It is reasonable to assume that the clusters were deposited during sample handling.

5.1.3 Configuration 2

A second configuration in which the collector was positioned above and parallel to the target sample during machining was developed (Figure 5.7). In this configuration, the collector taped to a teflon sheet about 1" away from the target sample using a T-stand. The target was taped onto the 3D stage.

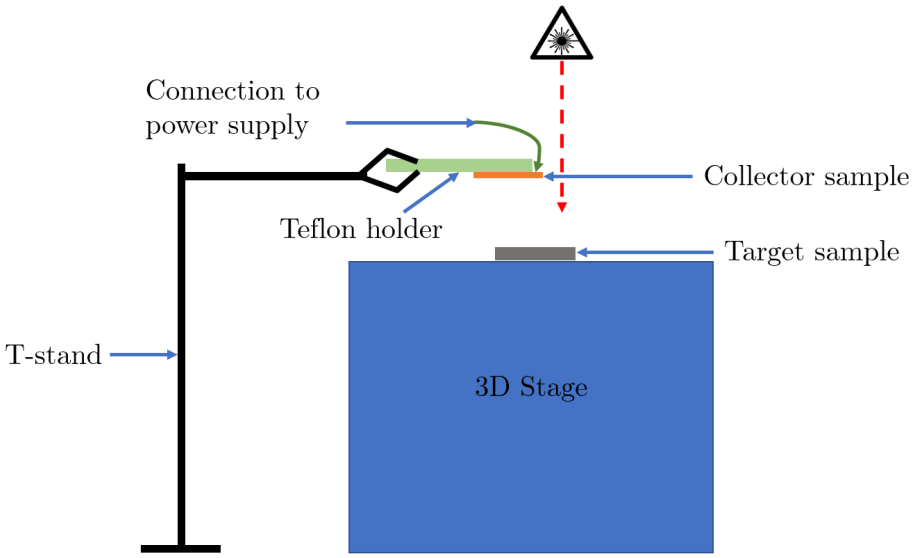

Figure 5.7: A schematic diagram of Configuration 2.

SEM was used to view the samples after the experiments and a few nanoparticles were found on the copper collector samples from the Ti/Cu pairs at +500 V and -500 V. Nanoparticles were not observed on the other collectors, but a web of nanoparticles as shown in Figure 5.8 formed between the target and the alligator clip connecting the collector to the power supply at high voltage (500 V) for both Ti/Cu and Cu/Ti pairs.

Table 5.3: A summary of the results from the experiments using Configuration 2.

Target/Collector Pair	**Collector Voltage(Cu)**	**Collected nps**
Ti/Cu	+500 V	minimal on collector; web on clip
Ti/Cu	-500 V	minimal on collector; web on clip
Ti/Cu	+100 V	no
Ti/Cu	-100 V	no
Cu/Ti	+500 V	on clip
Cu/Cu	-500 V	on clip
Cu/Ti	+100 V	no
Cu/Cu	-100 V	no

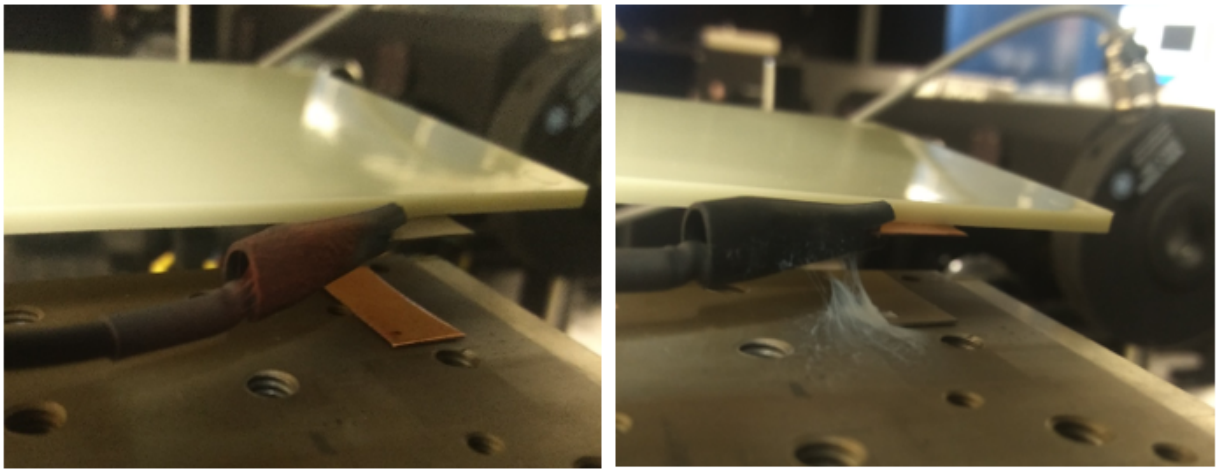

Figure 5.8: The 'web' of nanoparticles formed between the target sample (left: copper; right: titanium) and the alligator clip connecting the collector sample (left: titanium; right: copper) to the power supply.

Hence, the evidence suggested that the field enhancement at a point, such as the alligator clip or the corner of the collector sample, may have prevented collection on the surface area

of the collector. Moreover, this behaviour was not observed at 100 V, so higher voltage appeared to improve collection but the polarity had no influence.

5.1.4 Impact

The proof of concept experimens demonstrated the following:

1. Nanoparticles can be influenced by electric charge and increasing the voltage on the collector sample appears to increase the amount of nanoparticles collected.

2. Configuration 2 was more successful; any 3-D printed setup must be fixed to the 3-D stage with a screw to ensure stability.

3. Copper collectors appear to be more effective than titanium.

4. Field enhancement at the corner of the collector sample and the alligator clip can be reduced by placing the clip further away from the target and rounding the corners of the collectors.

5. An agglomeration of nanoparticles located beneath the patch machined on the target sample was observed in all the experiments; the particles are deposited in the direction of the machining trajectory.

5.2 Experiments

Based on the findings from the proof of concept tests, two new experiments were designed to focus on using high voltage supplied to titanium and copper collectors. The new setups would be fixed to the stage with screws to ensure stability during experiments and collectors would be connected to the power supply at a location far from the target material. All the samples (collectors and targets) had rounded corners to further reduce field enhancement. The titanium sheets were sanded and circular copper samples were punched using a die. As

done before, SEM was used to visualize the micromachined patches on the target samples and the nanoparticles on the collector samples.

To ensure that the proximity of the target to the collector did not affect the collection of nanoparticles, *un-charged* collector plates were positioned at distances of 1 cm, 2 cm, 3 cm, 4 cm, and 5 cm during micromachining experiments. Nanoparticles were not observed on any of the un-charged collector plates after these experiments.

5.2.1 Electric Field

In the proof of concept tests, it was established that supplying the target sample with a voltage with opposite polarity to the collector did not influence collection. The goal of this experiment was to determine if nanoparticles generated between two collectors with opposite polarity would have a different effect. Thus, an electric field was established between two collector plates and the target sample was placed between them, as demonstrated by Figure 5.9. In each experiment, collector A was the ground and collector B would be set to +/- 500 V (Table 5.4).

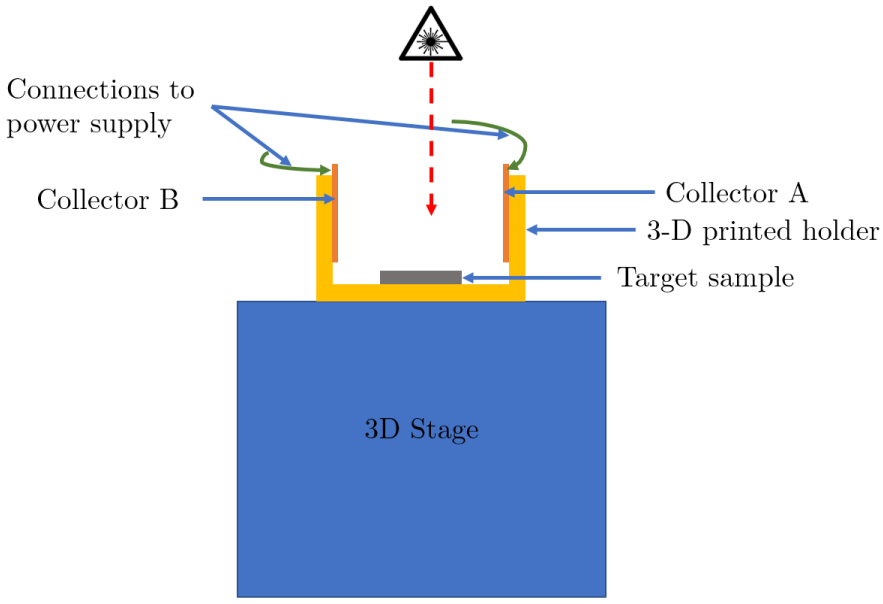

Figure 5.9: A schematic diagram of the configuration used for the electric field experiments.

Table 5.4: A summary of the experiments completed at 500 V with target samples place in an eletric field establishd between collectors A and B.

A/Target/B	**Collector B Polarity**	**Collected nps**
Ti/Ti/Ti	+	no
Ti/Ti/Ti	-	no
Cu/Ti/Cu	+	no
Cu/Ti/Cu	-	no
Ti/Cu/Ti	+	no
Ti/Cu/Ti	-	no
Cu/Cu/Cu	+	no
Cu/Cu/Cu	-	no

SEM images showed that there was no collection on any of the collectors from the electric field experiments. Nevertheless, there was little agglomeration of nanoparticles on the micro-machined patches (Figure 5.10 & 5.11). The nanoparticles were clustered beneath the patches micro-machined on titanium as in the proof of concept tests. The patches micro-machined on copper had less nanoparticles agglomerated beneath the patch and the nanoripple structure was visible at higher magnification on the patch itself.

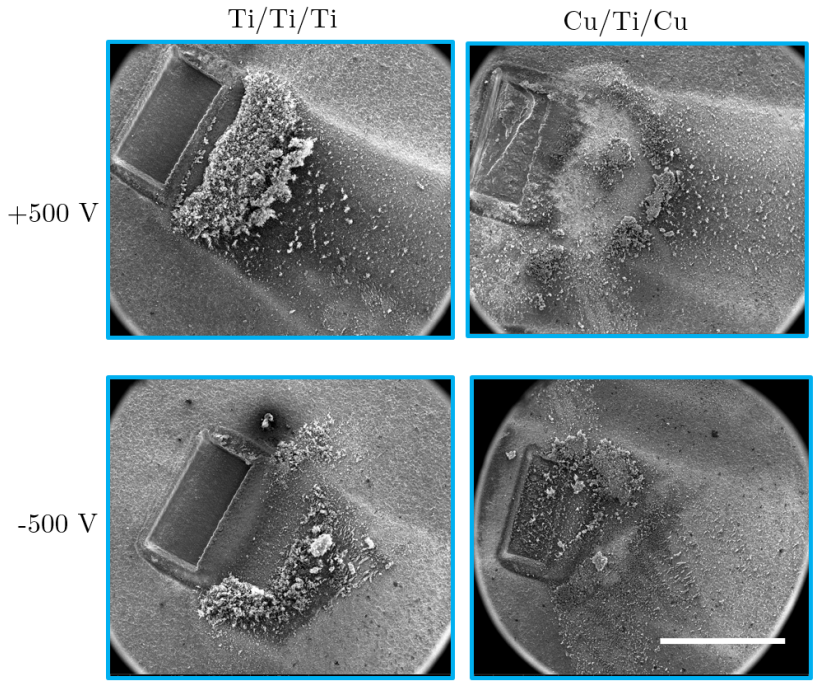

Figure 5.10: SEM images showing titanium samples placed in an electric field established between titanium collectors and copper collectors, scale is 1 mm.

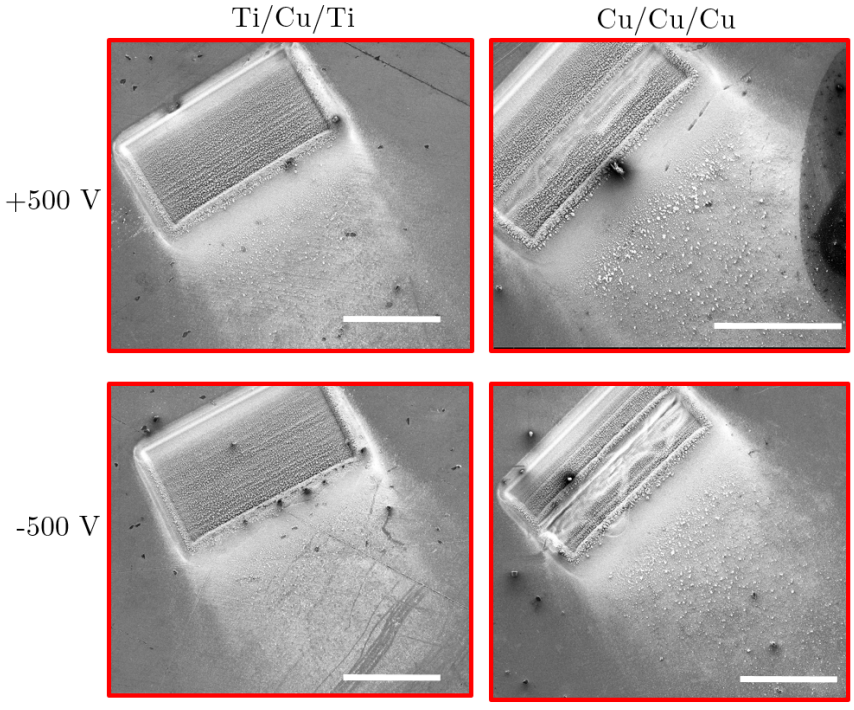

Figure 5.11: SEM images showing copper samples placed in an electric field established between titanium and copper collectors at 500 V. All length scales correspond to 500 μm.

5.2.2 Electric Charge

The proof of concept tests showed that the voltage of a collector plate would impact the amount of nanoparticles collected but the influence of material was not demonstrated. Thus, this series of experiments were conducted to determine whether the choice of target or collector material influence the collection process. Similar to the electric charge proof of concept experiments, the collector plate was placed 1" - 1.5" away from the target sample (Figure 5.12). The collector plate was bent into an L-shape to isolate the alligator clip connection to the power supply from the collection area. The experiments were conducted at 500 V (Table 5.5).

Table 5.5: A summary of the experiments completed at 500 V with target samples placed directly below Ti or Cu collector samples of varing polarity.

Target/Collector Pair	**Collector Polarity**	**Collected nps**
Ti/Ti	+	minimal
Ti/Ti	-	minimal
Ti/Cu	+	no
Ti/Cu	-	no
Cu/Ti	+	minimal
Cu/Ti	-	minimal
Cu/Cu	+	yes
Cu/Cu	-	yes

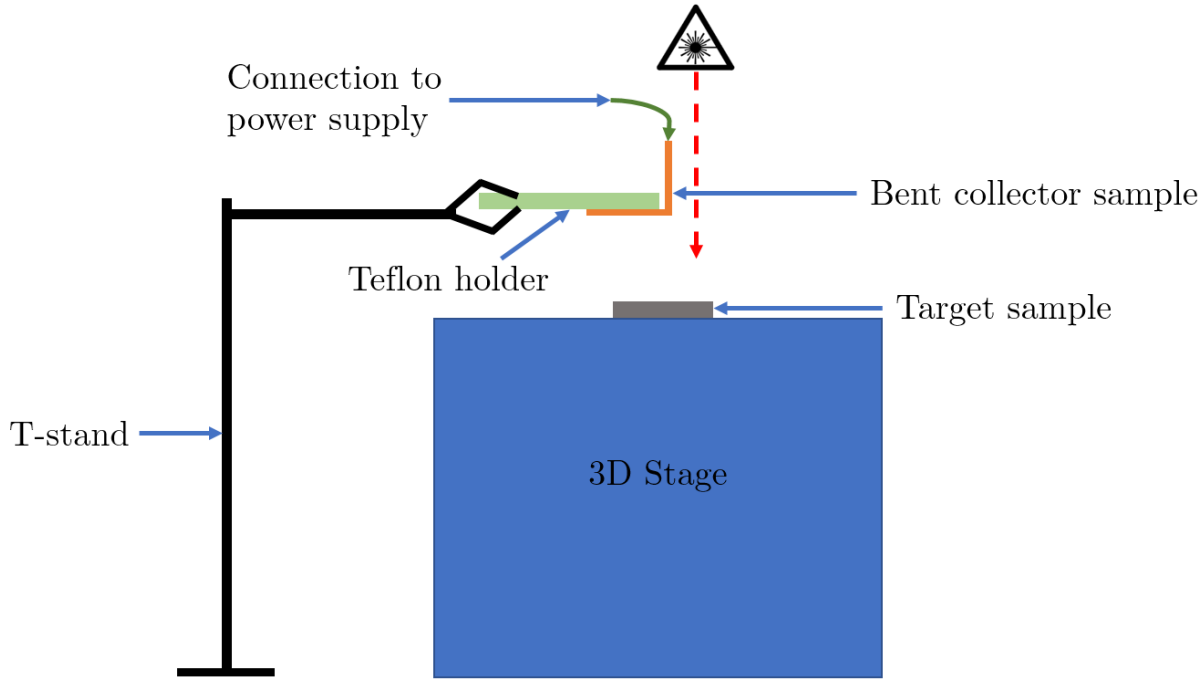

Figure 5.12: A schematic diagram of the configuration used for the electric charge experiments.

The SEM images (Figures 5.13 & 5.14) of the titanium target samples show significantly less nanoparticle accumulation at the bottom of the machined patch in comparison to Figure 5.10. There is very little nanoparticle deposition directly on the titanium patch. SEM (Figures 5.13 & 5.14) of the copper and titanium collectors show some collection of titanium nanoparticles at both +500 V and -500 V.

Similar to the copper samples placed in an electric field (Figure 5.11), the copper target samples show in Figures 5.15 & 5.16 have little accumulation of nanoparticles beneath the machined patch and the nano-ripple structure is visible at high magnification. In this case, SEM images of the titanium collectors showed copper nanoparticles at high magnification. However, the experiment proved most successful with the Cu/Cu pairs, where a web-like formation of copper nanoparticles is visible on the copper target surface (Figure 5.16). The polarity of the target surface did not affect the amount of collected nanoparticles.

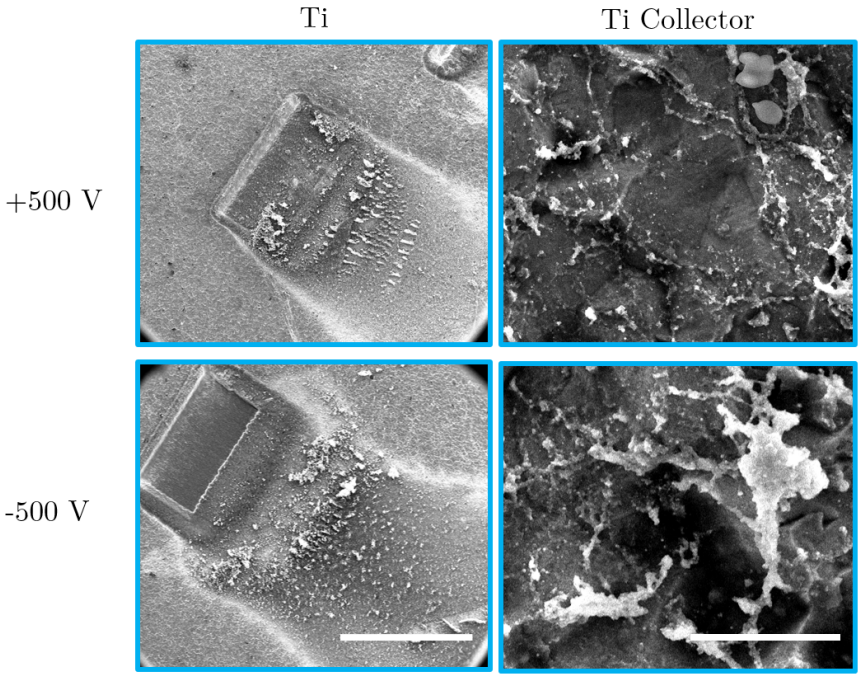

Figure 5.13: SEM images showing titanium samples (left) placed beneath titanium collectors (right) at +500 V and -500 V. Images of the titanium samples are of 1mm length scale and the collectors have length scale of 10 μm.

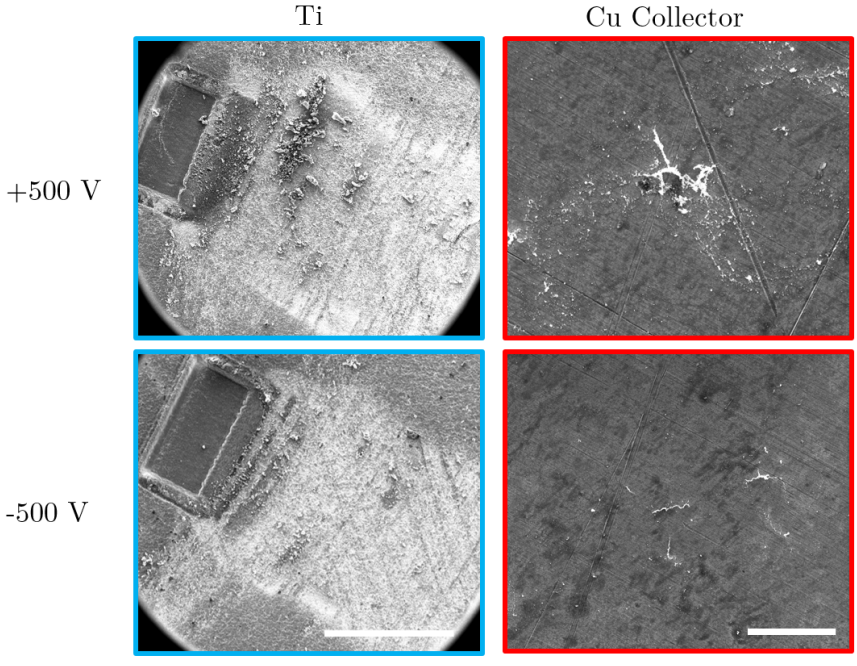

Figure 5.14: SEM images showing titanium samples (left, blue) placed beneath copper collectors (right, red)) at +500 V and -500 V. Images of the titanium samples are of 1mm length scale and the collectors have length scale of 50 μm.

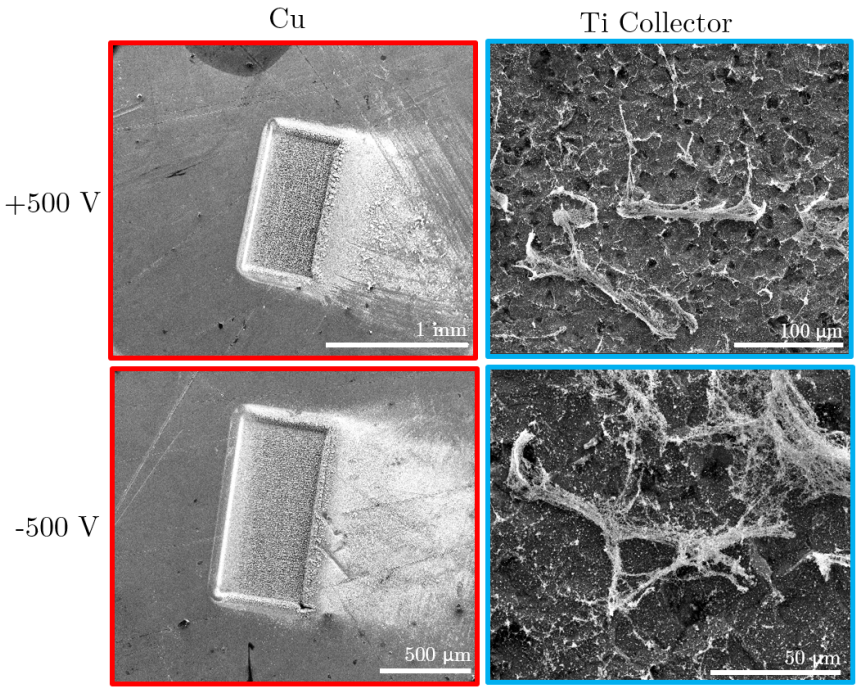

Figure 5.15: SEM images showing copper samples (left, red) placed beneath titanium collectors (right, blue) at +500 V and -500 V.

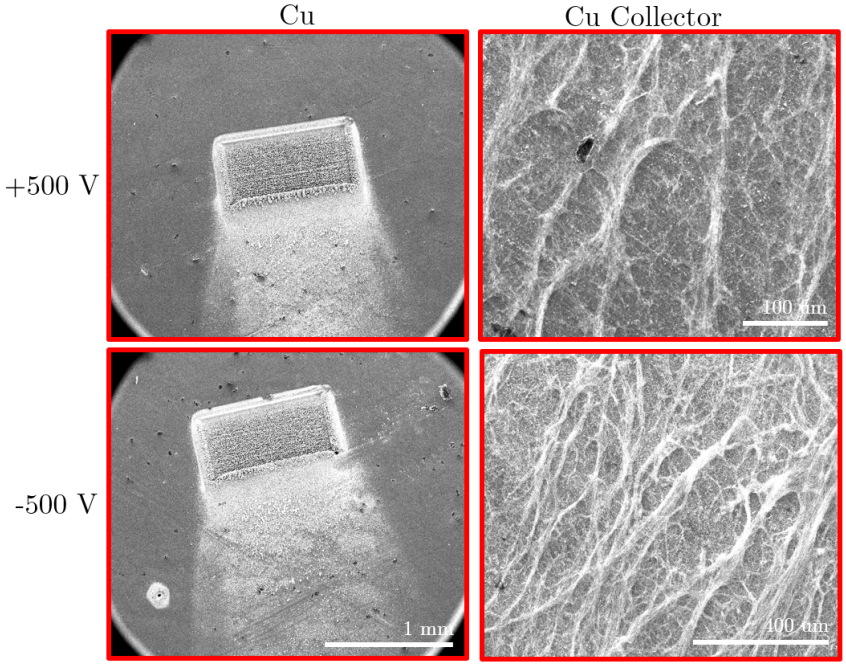

Figure 5.16: SEM images showing copper samples (left) placed opposite copper collectors (right) at +500 V and -500 V.

5.2.3 Discussion

Collection vs. Removal

Nanoparticles accumulated onto the collector surface during the electric charge experiments (Figures 5.13, 5.14, 5.15 & 5.16). However, the SEM images of the target samples from the electric field experiments showed little accumulation of nanoparticles on the machined patch (Figures 5.10 & 5.11). This behaviour was pronounced on the copper target samples in Figure 5.11. These results suggest that depending on the setup, nanoparticles may be removed from a target sample without accumulating on a collector surface.

Influence of Voltage & Charge

The proof of concept tests already confirmed that increasing the voltage supplied to the collector would in turn increase the amount of nanoparticles collected. The electric field and electric charge experiments demonstrated that the polarity of the collectors does not have an effect on collection. In fact, in the most successful cases (Cu/Cu pairs of electric charge experiments), copper nanoparticles were visible on collectors with positive and negative polarity.

Nanoparticle Trail

The agglomeration of nanoparticles beneath machined patches was observed on all the target samples. Moreover, during the proof of concept tests it became clear that the nanoparticles cluster in the direction of the machining trajectory. The proposed mechanism for this occurence is that during each line scan, generated nanoparticles decorate the sample surface on either side of the newly machined line. When scanning the next line, the laser beam will ablate both the surface and the layer of nanoparticles deposited from the earlier scan. The continuous deposition and ablation process results in a dusty surface trail left ahead of the

laser beam and a relatively clean one behind it.

Influence of Material

The results of this study demonstrate that the choice of target and collector material will impact the collection of nanoparticles. Specifically, in the electric charge experiments, copper nanoparticles sparsely covered the titanium collectors in comparison to copper collectors which had a thick web of nanoparticles (Figures 5.15 & 5.16). This supports the notion that a more conductive collector is more effective in attracting nanoparticles.

Mechanism of Nanoparticle Transport

The mechanism by which the nanoparticles are transported is not clear from the experiments completed in this thesis but there are two possible explanations for the observed behaviour. First, as suggested by other researchers (Barbosa et al., 2016; Ivlev et al., 2003; Li et al., 2009; Watanabe, 2006; Wang et al., 2014), nanoparticles may have a surface charge that causes an attraction to a collector. In this scenario, one would assume that nanoparticles are either postively or negatively charged. However, the results of this study indicate that when collection occurs it is not related to the polarity of the collector.

The second theory is that the nanoparticles are actually transported by the plasma generated on the surface of the micro-machined sample. When nanoparticles are generated in ambient environment, they are immediately oxidized and by extension, should have no charge. But plasma comprises of positive and negative ions that would be attracted to both a positively or negatively charged surface. It is thus possible that during micro-machining, the plasma is attracted to the collector and in a sense, pulls the nanoparticles with it towards the charged electrode. This is supported by the results where copper target samples had very little accumulation of nanoparticles on their surfaces even when the particles did not accumulate on a collector surface, as in the electric field experiments (Figure 5.11). Thus, if

the plasma is the entity that is manipulated in the presence of a collector, nanoparticles can be removed from a target without being collected. Nevertheless, more experiments must be conducted to clarify the mechanism of nanoparticle transport.

Chapter 6: Conclusion

6.1 Conclusions from Chamber Design and SOP Development

After developing possible chamber designs for controlled environment experiments, a prototype chamber was assembled using readily available parts. Testing the prototype in a variety of conditions informed the design and assembly of the final chamber, and highlighted necessary SOP steps for smooth operation of this chamber in future experiments. Upon re-evaluation of the proposed chamber designs and studying the limitations of a prototype chamber, it is clear that the cube design is the most suitable for laser micro-machining in gas and vacuum environments. The final design accomodates up to four samples, fits within the space limitations of the 3-D translation stage and the glove box, and its compact shape reduces the likelihood of damage to the stage. Moreover, the sapphire window is less prone to browning and there are two ports that can be used for future customizations such as a viewing window or pressure gauge.

The development of an SOP for future experiments outlined key techniques for using the apparatuses and sample handling. It is important that the sample holder inside the chamber is always in the same location to ensure that there is no misalignment with the lens. As well, sample surface compositions are highly sensitive to oils and dust, so researchers should always handle samples with gloves and clean the surface with acetone immediately before

experiments. Finally, the X-ray spot size in the XPS apparatus should always be adjusted to the surface topography characteristic sizes.

6.2 Conclusions from the Nanoparticle Collection

Nanoparticle accumulation on samples, chamber walls and window was observed during prototype experiments, thus methods for nanoparticle collection or removal were explored. Preliminary experiments to test whether nanoparticles have a surface charge that can be manipulated for transport proved that in the presence of a charged collector, nanoparticles can be transported due to an attraction to the collector. Copper collectors were more effective than titanium at attracting both copper and titanium nanoparticles. The voltage and choice of material will influence the amount of nanoparticles collected but the polarity of the collector was not shown to have an effect. It was also shown that nanoparticles will accumulate on the target sample in the direction of the machining trajectory.

Although, the nanoparticles were transported in the experiments, there is a question of whether said transport is a result of the nanoparticle surface charge or the plasma environment. Further studies will illuminate the mechanism of the transport.

Chapter 7: Original Contributions

The independent and original contributions made to this thesis are as follows:

1. A prototype apparatus was designed and built for laser micromachining experiments and surface chemistry analysis in an XPS apparatus. The prototype successfully enabled preliminary experiments in gas and vacuum environments.

2. A technique for removing nanoparticles from laser micromachined surfaces during experiments was developed.

Chapter 8: Further Work

1. **Improvements to the Final Chamber Design**

   The current design does not include parts for gas flow or pressure control, but it can be modified for such purposes for future experiments. Flanges can be fabricated by welding pressure gauges to off-the shelf flange caps with help from the Chemical Engineering machine shop. A rotameter can be fitted to the gas line to measure flow rates as a low-cost option. A more sophisticated but expensive approach would be a mass flow controller. In order to view experiments, a kodial glass window can be purchased from Kurt J Lesker or MDC Vacuum and fastened to one of the two available ports. It is important to note that the window(s) must be cleaned frequently to prevent nanoparticle build-up and signs of 'browning' should be monitored. As well, all modifications should be within the weight (<3.8 kg) and balance limitations of the 3-D stage.

2. **Nanoparticles Experiments**

   The experimental design to ascertain the mechanism of nanoparticle transport in the presence of an electric charge must include a method to monitor the movement of the nanoparticles and a method to determine that the phenomenon only occurs with conductive materials. The proposed experiments are:

   (a) Using a high speed camera to monitor the laser micromachining of a copper plate in the presence of a charged copper collector. In previous experiments at the

BSEL (Paolasini and Kietzig, 2014), the high speed camera has been employed in monitoring the plasma plume expansion during fs laser micro-machining. A similar experiment with the charged copper plate would demonstrate if changes occur to the plasma plume in the presence of charge and possibly depict the movement of the nanoparticles.

(b) Laser micromachining of a PTFE plate in the presence of a charged copper plate. Machining an insulative material should generate insulative nanoparticles, which should serve as a more suitable control for the *surface charge* hypothesis of metal nanoparticles. The PTFE nanoparticles have no net charge, thus they will not be attracted or repelled by a metal collector plate. If the experiments show that there is collection of teflon nanoparticles on a metal collector, it would suggest that the driving force for collection comes from the plasma.

(c) Inductive Coupled Plasma - Atomic Electron Spectroscopy (ICP-AES) analysis can be used as a method for determining the amount of nanoparticles generated and successfully removed from a sample. Such a procedure would be useful in quantifying the efficiency of different collectors in *collecting* nanoparticles.

(d) A comparison of micromachined samples with accumulation of nanoparticles beneath the patches, with and without the presence of a charged collector. Specifically, taking a look at the amount of nanoparticles *removed* could further illuminate the transport mechanism of nanoparticles.

Bibliography

K. M. Tanvir Ahmmed. Introducing a new optimization tool for femtosecond laser-induced surface texturing on titanium, stainless steel, aluminum and copper. *Optics and Lasers in Engineering*, 66:258–268, 2015a. ISSN 0143-8166.

K. M. Tanvir Ahmmed. Introducing a new optimization tool for femtosecond laser-induced surface texturing on titanium, stainless steel, aluminum and copper. *Optics and Lasers in Engineering*, 66:258–268, 2015b. ISSN 0143-8166.

KM Ahmmed, Colin Grambow, and Anne-Marie Kietzig. Fabrication of micro/nano structures on metals by femtosecond laser micromachining. *Micromachines*, 5(4):1219–1253, 2014.

T. Baldacchini, J. E. Carey, M. Zhou, and E. Mazur. Superhydrophobic surfaces prepared by microstructuring of silicon using a femtosecond laser. *Langmuir : the ACS journal of surfaces and colloids*, 22(11):4917–9, 2006. ISSN 0743-7463.

S. Barbosa, L. Couëdel, C. Arnas, K. Kishor Kumar, C. Pardanaud, and F. R. A. Onofri. In-situ characterisation of the dynamics of a growing dust particle cloud in a direct-current argon glow discharge. *Journal of Physics D: Applied Physics*, 49(4):045203, 2016. ISSN 0022-3727. URL http://stacks.iop.org/0022-3727/49/i=4/a=045203.

L. Bergé, S. Skupin, R. Nuter, J. Kasparian, and J. P. Wolf. Ultrashort filaments of light in weakly ionized, optically transparent media. *Reports on Progress in Physics*, 70(10):1633, 2007. ISSN 0034-4885. URL http://stacks.iop.org/0034-4885/70/i=10/a=R03.

Priyanka Bhattacharya, Smita Gohil, Javed Mazher, Shankar Ghosh, and Pushan Ayyub. Universal, geometry-driven hydrophobic behaviour of bare metal nanowire clusters. *Nanotechnology*, 19(7):075709, 2008. URL http://stacks.iop.org/0957-4484/19/i=7/a=075709.

Sanchari Biswas, Adya Karthikeyan, and Anne-Marie Kietzig. Effect of repetition rate on femtosecond laser-induced homogenous microstructures. *Materials*, 9(12):1023, 2016.

P. Bizi-Bandoki. Modifications of roughness and wettability properties of metals induced by femtosecond laser treatment. *Applied Surface Science*, 257(12):5213–18, 2011. ISSN 0169-4332 0169-4332.

Pavel Bizi-Bandoki, Stephane Valette, Eric Audouard, and Stéphane Benayoun. Time dependency of the hydrophilicity and hydrophobicity of metallic alloys subjected to femtosecond laser irradiations. *Applied Surface Science*, 273:399–407, 2013. ISSN 0169-4332.

Marijus Brikas, Paulius Gecys, Mindaugas Gedvilas, and Gediminas Raciukaitis. *Accumulation effects in laser ablation of metals with high-repetition rate lasers*, volume 7005. 2008. doi: 10.1117/12.782937.

Feng-Ming Chang, Shao-Liang Cheng, Siang-Jie Hong, Yu-Jane Sheng, and Heng-Kwong Tsao. Superhydrophilicity to superhydrophobicity transition of cuo nanowire films. *Applied Physics Letters*, 96(11):114101, 2010. ISSN 0003-6951.

Jian Cheng, Chang-sheng Liu, Shuo Shang, Dun Liu, Walter Perrie, Geoff Dearden, and Ken Watkins. A review of ultrafast laser materials micromachining. *Optics & Laser Technology*, 46:88–102, 2013. ISSN 0030-3992.

Laurent Courbin and Howard A Stone. Your wetting day. *Physics Today*, 60(2):84–85, 2007. ISSN 0031-9228.

C. W. Extrand. Contact angles and hysteresis on surfaces with chemically heterogeneous islands. *Langmuir*, 19(9):3793–3796, 2003. ISSN 0743-7463. doi: 10.1021/la0268350. URL http://dx.doi.org/10.1021/la0268350.

Wenyan Geng, Anmin Hu, and Ming Li. Super-hydrophilicity to super-hydrophobicity transition of a surface with ni micro–nano cones array. *Applied Surface Science*, 263:821–824, 2012. ISSN 0169-4332. doi: http://dx.doi.org/10.1016/j.apsusc.2012.09.006. URL http://www.sciencedirect.com/science/article/pii/S0169433212015140.

Wolfgang Husinsky, Chandra SR Nathala, Sergey V Makarov, and Narjis Begum. Effect of fluence and ambient environment on the surface and structural modification of femtosecond laser irradiated ti. 2016.

John C. Ion. *Chapter 4 - Systems for Material Processing*, pages 104–138. Butterworth-Heinemann, Oxford, 2005. ISBN 978-0-7506-6079-2. doi: http://doi.org/10.1016/B978-075066079-2/50007-6. URL http://www.sciencedirect.com/science/article/pii/B9780750660792500076.

A. V. Ivlev, M. Kretschmer, M. Zuzic, G. E. Morfill, H. Rothermel, H. M. Thomas, V. E. Fortov, V. I. Molotkov, A. P. Nefedov, A. M. Lipaev, O. F. Petrov, Yu M. Baturin, A. I. Ivanov, and J. Goree. Decharging of complex plasmas: First kinetic observations. *Physical Review Letters*, 90(5):055003, 2003. URL https://link.aps.org/doi/10.1103/PhysRevLett.90.055003.

R. Jagdheesh, B. Pathiraj, E. Karatay, G. R. B. E. Römer, and A. J. Huis in't Veld. Laser-induced nanoscale superhydrophobic structures on metal surfaces. *Langmuir*, 27(13):8464–8469, 2011. ISSN 0743-7463. doi: 10.1021/la2011088. URL http://dx.doi.org/10.1021/la2011088.

Rulon E. Johnson and Robert H. Dettre. *Contact Angle Hysteresis*, volume 43 of *Advances in Chemistry*, book section 7, pages 112–135. AMERICAN CHEMICAL SOCIETY, 1964. ISBN 0-8412-0044-0. doi: doi:10.1021/ba-1964-0043.ch00710.1021/ba-1964-0043.ch007. URL http://dx.doi.org/10.1021/ba-1964-0043.ch007.

Anne-Marie Kietzig, Savvas G Hatzikiriakos, and Peter Englezos. Patterned superhydrophobic metallic surfaces. *Langmuir*, 25(8):4821–4827, 2009. ISSN 0743-7463.

Anne-Marie Kietzig, Mehr Negar Mirvakili, Saeid Kamal, Peter Englezos, and Savvas G Hatzikiriakos. Laser-patterned super-hydrophobic pure metallic substrates: cassie to wenzel wetting transitions. *Journal of Adhesion Science and Technology*, 25(20):2789–2809, 2011. ISSN 0169-4243.

Anne-Marie Kietziga, Mehr Negar Mirvakilia, Saeid Kamalb, Peter Englezosa, and Savvas G. Hatzikiriakosa. Nanopatterned metallic surfaces: Their wettability and impact on ice friction. *Journal of Adhesion Science and Technology*, 25(12):1293–1303, 2011. ISSN 0169-4243. doi: 10.1163/016942411X555872. URL http://dx.doi.org/10.1163/016942411X555872.

Doogon Kim, Jang Gil Kim, and Chong Nam Chu. Aging effect on the wettability of stainless steel. *Materials Letters*, 170:18–20, 2016. ISSN 0167-577X. doi: http://dx.doi.org/10.1016/j.matlet.2016.01.107. URL http://www.sciencedirect.com/science/article/pii/S0167577X16301070.

D. M. Krol. Femtosecond laser modification of glass. *Journal of Non-Crystalline Solids*, 354(2–9):416–424, 2008. ISSN 0022-3093. doi: http://dx.doi.org/10.1016/j.jnoncrysol.2007.01.098. URL http://www.sciencedirect.com/science/article/pii/S0022309307010836.

Jorge Lehr. *Capillary forces on femtosecond laser micromachined metallic surfaces*. Thesis, 2015. URL http://digitool.Library.McGill.CA:80/R/-?func=dbin-jump-full&object_id=132795&silo_library=GEN01'.

Jorge Lehr, Fabrizio de Marchi, Luke Matus, Jennifer MacLeod, Federico Rosei, and Anne-Marie Kietzig. The influence of the gas environment on morphology and chemical composition of surfaces micro-machined with a femtosecond laser. *Applied Surface Science*, 320:455–465, 2014. ISSN 0169-4332.

Lei Lei, Hao Li, Jian Shi, and Yong Chen. Diffraction patterns of a water-submerged superhydrophobic grating under pressure. *Langmuir*, 26(5):3666–3669, 2010. ISSN 0743-7463. doi: 10.1021/la903150h. URL http://dx.doi.org/10.1021/la903150h.

Paul Leiderer, Michael Olapinski, Mario Mosbacher, and Johannes Boneberg. Nanoparticle adhesion and removal studied by pulsed laser irradiation. In *High-Power Laser Ablation 2006*, pages 62610F–62610F–9. International Society for Optics and Photonics.

Yang-fang Li, U. Konopka, K. Jiang, T. Shimizu, H. Höfner, H. M. Thomas, and G. E. Morfill. Removing dust particles from a large area discharge. *Applied Physics Letters*, 94

(8):081502, 2009. doi: 10.1063/1.3089873. URL http://aip.scitation.org/doi/abs/10.1063/1.3089873.

Edwin Jee Yang Ling, Victor Uong, Jean-Sébastien Renault-Crispo, Anne-Marie Kietzig, and Phillip Servio. Reducing ice adhesion on nonsmooth metallic surfaces: Wettability and topography effects. *ACS Applied Materials & Interfaces*, 8(13):8789–8800, 2016. ISSN 1944-8244. doi: 10.1021/acsami.6b00187. URL http://dx.doi.org/10.1021/acsami.6b00187.

Peng Liu, Ling Cao, Wei Zhao, Yue Xia, Wei Huang, and Zelin Li. Insights into the superhydrophobicity of metallic surfaces prepared by electrodeposition involving spontaneous adsorption of airborne hydrocarbons. *Applied Surface Science*, 324:576–583, 2015. ISSN 0169-4332. doi: http://dx.doi.org/10.1016/j.apsusc.2014.10.170. URL http://www.sciencedirect.com/science/article/pii/S0169433214024362.

X Liu, D Du, and G Mourou. Laser ablation and micromachining with ultrashort laser pulses. *IEEE journal of quantum electronics*, 33(10):1706–1716, 1997. ISSN 0018-9197.

Jiangyou Long, Minlin Zhong, Hongjun Zhang, and Peixun Fan. Superhydrophilicity to superhydrophobicity transition of picosecond laser microstructured aluminum in ambient air. *Journal of colloid and interface science*, 441:1–9, 2015. ISSN 0021-9797.

Florian Merkt. *Interactions of nanoparticles and surfaces*. Thesis, 2008.

JP Michel, M Beauverger, L Museur, A Kanaev, and JP Petitet. High-pressure cell for studies of ultra-short laser impulses action on materials. *High Pressure Research*, 27(3):353–359, 2007. ISSN 0895-7959.

Sanjay Mishra and Vinod Yadava. Laser beam micromachining (lbmm)–a review. *Optics and Lasers in Engineering*, 73:89–122, 2015. ISSN 0143-8166.

M. D. Murthy Peri, Ivin Varghese, and Cetin Cetinkaya. *Chapter 3 - Laser Cleaning for Removal of Nano/Micro-Scale Particles and Film Contamination*, pages 63–122. William Andrew Publishing, Oxford, 2011. ISBN 978-1-4377-7885-4. doi: http://doi.org/10.1016/B978-1-4377-7885-4.10003-X. URL http://www.sciencedirect.com/science/article/pii/B978143777885410003X.

B. K. Nayak. Formation of nano-textured conical microstructures in titanium metal surface by femtosecond laser irradiation. *Applied Physics A : Materials Science and Processing*, 90(3):399–402, 2008. ISSN 1432-0630 0947-8396.

Steven Paolasini and Anne Kietzig. Synchronized videography of plasma plume expansion during femtosecond laser ablation. In *Laser Applications in Microelectronic and Optoelectronic Manufacturing (LAMOM) XIX*, volume 8967, page 896710. International Society for Optics and Photonics, 2014.

W. Perrie, M. Gill, G. Robinson, P. Fox, and W. O'Neill. Femtosecond laser micro-structuring of aluminium under helium. *Applied Surface Science*, 230(1):50–59, 2004. ISSN 0169-4332.

doi: https://doi.org/10.1016/j.apsusc.2003.12.035. URL http://www.sciencedirect.com/science/article/pii/S016943320400008X.

H. Rathgen. Microscopic shape and contact angle measurement at a superhydrophobic surface. *Faraday Discussions*, 146:49–56, 2010. ISSN 1364-5498 1359-6640.

G. M. Robinson and M. J. Jackson. Femtosecond laser micromachining of aluminum surfaces under controlled gas atmospheres. *Journal of Materials Engineering and Performance*, 15(2):155–160, 2006. ISSN 1544-1024. doi: 10.1361/105994906x95805. URL https://doi.org/10.1361/105994906X95805.

Kwangseok Seo, Minyoung Kim, and Do Hyun Kim. *Re-derivation of Young's Equation, Wenzel Equation, and Cassie-Baxter Equation Based on Energy Minimization*, page Ch. 01. InTech, Rijeka, 2015. doi: 10.5772/61066. URL http://dx.doi.org/10.5772/61066.

L. A. Siiman, J. Lumeau, and L. B. Glebov. Nonlinear photoionization and laser-induced damage in silicate glasses by infrared ultrashort laser pulses. *Applied Physics B*, 96(1):127–134, 2009. ISSN 1432-0649. doi: 10.1007/s00340-009-3526-8. URL http://dx.doi.org/10.1007/s00340-009-3526-8.

Dongbo Wang, Jing Ye, Steven D. Hudson, Keana C. K. Scott, and Sheng Lin-Gibson. Effects of nanoparticle size and charge on interactions with self-assembled collagen. *Journal of Colloid and Interface Science*, 417:244–249, 2014. ISSN 0021-9797. doi: http://dx.doi.org/10.1016/j.jcis.2013.11.019. URL http://www.sciencedirect.com/science/article/pii/S0021979713010035.

Y. Watanabe. Formation and behaviour of nano/micro-particles in low pressure plasmas. *Journal of Physics D: Applied Physics*, 39(19):R329, 2006. ISSN 0022-3727. URL http://stacks.iop.org/0022-3727/39/i=19/a=R01.

Robert N. Wenzel. Resistance of solid surfaces to wetting by water. *Industrial & Engineering Chemistry*, 28(8):988–994, 1936. ISSN 0019-7866. doi: 10.1021/ie50320a024. URL http://dx.doi.org/10.1021/ie50320a024.

Long Yin, Lin Zhu, Qingjun Wang, Jianfu Ding, and Qingmin Chen. Superhydrophobicity of natural and artificial surfaces under controlled condensation conditions. *ACS Applied Materials & Interfaces*, 3(4):1254–1260, 2011. ISSN 1944-8244. doi: 10.1021/am200061t. URL http://dx.doi.org/10.1021/am200061t.

Long Yin, Yuanyi Wang, Jianfu Ding, Qingjun Wang, and Qingmin Chen. Water condensation on superhydrophobic aluminum surfaces with different low-surface-energy coatings. *Applied Surface Science*, 258(8):4063–4068, 2012. ISSN 0169-4332. doi: http://dx.doi.org/10.1016/j.apsusc.2011.12.100. URL http://www.sciencedirect.com/science/article/pii/S0169433211020162.

Yingchuan Zhang, Guisheng Zou, Lei Liu, Yue Zhao, Qiong Liang, Aiping Wu, and Y. Norman Zhou. Time-dependent wettability of nano-patterned surfaces fabricated by femtosecond laser with high efficiency. *Applied Surface Science*, 389:554–559, 2016. ISSN 0169-4332.

doi: http://dx.doi.org/10.1016/j.apsusc.2016.07.089. URL http://www.sciencedirect.com/science/article/pii/S0169433216315252.

V. P. Zhukov and N. M. Bulgakova. Role of ambient gas in heating of metal samples by femtosecond pulses of laser radiation. *Thermophysics and Aeromechanics*, 16(2):165–176, 2009. ISSN 1531-8699. doi: 10.1134/s0869864309020012. URL http://dx.doi.org/10.1134/S0869864309020012.

V. Zorba, L. Persano, D. Pisignano, A. Athanassiou, E. Stratakis, R. Cingolani, P. Tzanetakis, and C. Fotakis. Making silicon hydrophobic: wettability control by two-lengthscale simultaneous patterning with femtosecond laser irradiation. *Nanotechnology*, 17(13):3234, 2006. ISSN 0957-4484. URL http://stacks.iop.org/0957-4484/17/i=13/a=026.

Vassilia Zorba. Biomimetic artificial surfaces quantitatively reproduce the water repellency of a lotus leaf. *Advanced Materials*, 20(21):4049–4054, 2008. ISSN 1521-4095 0935-9648.

Appendices

Appendix A: Standard Operating Procedures

A.1 Prototype Chamber

A.1.1 Finding the home position of the stage with the chamber

- Move the stages to the home position (i.e. 0,0,0).
- Place the reflective paper on the chamber window and mark the center position.
- With the laser on low power (just enough to be visible on the reflective paper), open the shutter and check whether the paper is in the beam path.
- Move the stages until the beam is more or less at the spot you marked on the reflective paper. Note the x, y and if necessary, z coordinates of the position because this will be the new home position for all machining experiments.
- Always bring the stages to (0,0,0), then start your machining program which will bring the stages to your 'new home position' before starting your experiment.
- I recommend doing a few test experiments to ensure that your patch or lines are properly machined before starting your experiments. Minor misalignments can affect the beam path, thus preventing proper machining.

A.1.2 Sample Preparation & Loading

- Before starting experiments, determine the focus position of the laser beam on your sample when taped to the make-shift stage inside the chamber. See the 'Focus' document in the BSEL Dropbox folder titled 'SOP & Safety'.
- Note that the laser beam does not always pass directly through the centre of the chamber window. So, you must ensure that your sample is in the beam path when loading it into the chamber. I suggest marking the LEGO® stage with your desired position to reduce error.
- Samples should be prepared according to the requirements of the experiments being carried out (i.e. cutting, polishing and sonication). The sample is loaded through the chamber's flange, it cannot exceed the 1.25" radius available.

- Immediately before loading into the chamber, samples should be wiped again with acetone. Doing this will ensure a pristine surface free of dust and other contaminants. For controlled environment experiments, handle your samples with gloves and tweezers to prevent contamination.
- The sample should be secured onto the LEGO® stage with double-sided tape.
- The window, butterfly valve, swagelok fitted flange and bottom flange must be attached to the chamber with an o-ring and a clamp
- Also, when screwing the chamber into the 3-D translation stage, keep in mind that you always want the chamber to be perfectly centered. This will reduce imbalances on the 3-D stage and ensure that the gas and/or vacuum lines are not obstructing other items on the laser table.

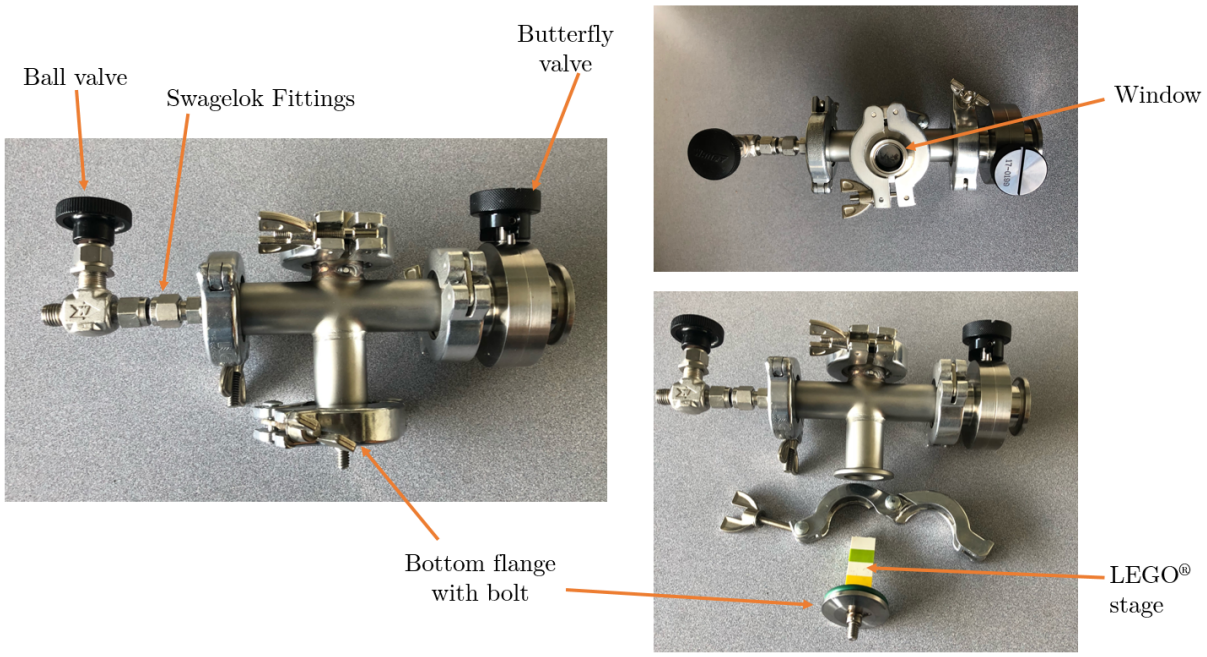

Figure A.1: The assembly of the prototype is shown above

A.1.3 Connecting to Gas & Vacuum Lines

- Once the chamber is screwed correctly into the 3-D stage, clamp the butterfly valve the chamber and open it. Then connect the vacuum pump to the valve with the rigid stainless steel tube.
- If you are running an experiment under vacuum, ensure that the ball valve on the gas line is closed. Then turn on the vacuum pump and wait a couple of minutes. Ensure that there are no leaks in the system and the 3-D stage is balanced before starting your experiment.

- If you are running an experiment under gas flow, connect the gas line to the flange on the other side via the ball valve. Do not open the ball valve yet.
- Before feeding gas through the system, turn on the vacuum pump and wait a couple of minutes. Ensure that there are no leaks and the 3-D stage is balanced. If the 3-D stage is encountering a balance problem, it will make a high-pitched screech or whine.
- If everything is secured, open the ball valve about halfway. Then, open the main valve on the gas cylinder to the desired pressure. Ensure that the pressure is not too high for the vacuum pump. If too much gas is being fed into the system, the pump will sputter and may stop working so PAY ATTENTION.
- When the lines are connected and running correctly, you can begin your experiment.
- Once the experiment is completed, shut off the gas line by closing the main valve on the gas cylinder and then closing the ball valve tightly. Disconnect the gas line from the system.
- Close the butterfly valve and shut off the vacuum pump. Disconnect the rigid tubing from the system.
- Do not remove the valves! Just close them.
- Carefully unscrew the chamber from the 3-D stage and carry it to the glove box.

A.2 Cube Chamber

A.2.1 Sample Preparation & Loading

- Samples can be prepared in the same way outlined in A.1.2. If you would like to load four samples onto the sample holder, ensure that your target area is $\leq$2.2 cm in length and width.
- Using an adjustable wrench, removing the nuts and bolts that attach the bottom flange to the cube chamber.
- Remove the sample holder and place your samples in marked locations. Place the sample holder back on the flange and re-attach the flange using the nuts and bolts. Remember to replace the o-ring.
- Note that each sample location on the holder is marked A, B, C or D. Be aware of where your samples are placed.
- After bolting the other flanges onto the cube frame, bolt the chamber holder to the 3-D translation stage and place the chamber in its holder.
- Home the 3D stage to (0,0,0).
- Remember to include the sample locations (A, B, C or D) in your machining trajectory.

A.2.2 Connecting to Gas and Vacuum Lines

- Once the chamber is in position on the 3D stage, connect the gas line to the ball valve connection. Clamp the butterfly valve to the flange end of the PTFE-SS mesh tube and open the valve.
- Clamp the other end of the butterfly valve to the rigid tubing from the vacump pump.
- If you're running an experiment under vacuum, ensure that the ball valve on the gas line is closed. Then turn on the vacuum pump and wait a couple of minutes. Ensure that there are no leaks in the system and the 3-D stage is balanced before starting your experiment.
- If you're running an experiment under gas flow, connect the gas line to the flange on the other side via the ball valve. Do not open the ball valve yet.
- Before feeding gas through the system, turn on the vacuum pump and wait a couple of minutes. Ensure that there are no leaks and the 3-D stage is balanced. If the 3-D stage is encountering a balance problem, it will make a high-pitched screech or whine.
- If everything is secured, open the ball valve about halfway. Then, open the main valve on the gas cylinder to the desired pressure. Ensure that the pressure is not too high for the vacuum pump. If too much gas is being fed into the system, the pump will sputter and may stop working so PAY ATTENTION.
- When the lines are connected and running correctly, you can begin your experiment.
- Once the experiment is completed, shut off the gas line by closing the main valve on the gas cylinder and then closing the ball valve tightly. Disconnect the gas line from the system.
- Close the butterfly valve and shut off the vacuum pump. Disconnect the rigid tubing from the system. NOTE: you should only disconnect the rigid tubing from the vacuum pump. The butterfly valve and PTFE-SS mesh tube should remain attached.
- Do not remove the valves! Just close them.
- Remove the chamber from its holder carefully witht he PTFE-SS mesh tube and butterfly valve. Carry the system to the glove box.

A.3 Analysis

A.3.1 Transfer into VTM in glove box

- Be sure to book the glove box with the PPL before using it. This will ensure that sensitive experiments or samples are not in the glove box during your time.
- Open the transfer port and fill the tray with the chamber, VTM, sample clips for the VTM, VTM lock pins and tweezers. Close the port.

- Evacuate and re-fill the transfer port three times, waiting a few seconds between evacuating and filling. At the end of this cycle, close the gas valve.
- Check that the O_2 concentration is <0.1 ppm.
- If the glove box light is off, you can turn it on by pressing 'Functions', 'Boxlight' and 'END' on the control touchpad.
- Enter the glove box slowly while pushing the low pressure pedal as you enter.
- Unload all the pieces from the transfer port into the glove box. Check that the O_2 concentration is still <0.1 ppm.
- Close the internal transfer port door.
- Unload the samples from the chamber and carefully attach them with clips to the VTM sample holder.
- Close the VTM with its cover and ensure that it is sealed properly (FRONT labels must match). Hold the cover in place with the retaining plate, screwing the pins until the cover is secure but not too tight.
- Place the VTM in the transfer port and evacuate it. Wait 2 minutes.
- Refill the transfer port and close the valve.
- Unload the sealed VTM into the glove box, remove the lock pins and check that it is evacuated.
- Place all the items back into the transfer port and remove them.
- Turn OFF the glove box light.

A.3.2 Notes on the VTM & XPS Apparatus

- The VTM can hold vacuum for up to 3 hours, so XPS analysis must occur within this time period. If you are not ready for XPS, leave the VTM in the glove box. This will prevent exposure to the ambient environment in the event that the VTM opens.
- It is good practice to clean the VTM before and after use. Wipe the VTM sample holder, o-ring and window with ethanol.
- If you hear a POP sound while evacuating the VTM in the transfer port, the VTM has re-opened. In this case, refill the transfer port, close the gas valve and unload the VTM into the glove box. Follow the instructions on closing the VTM and try evacuating again. Be sure to not screw the pins too tightly!

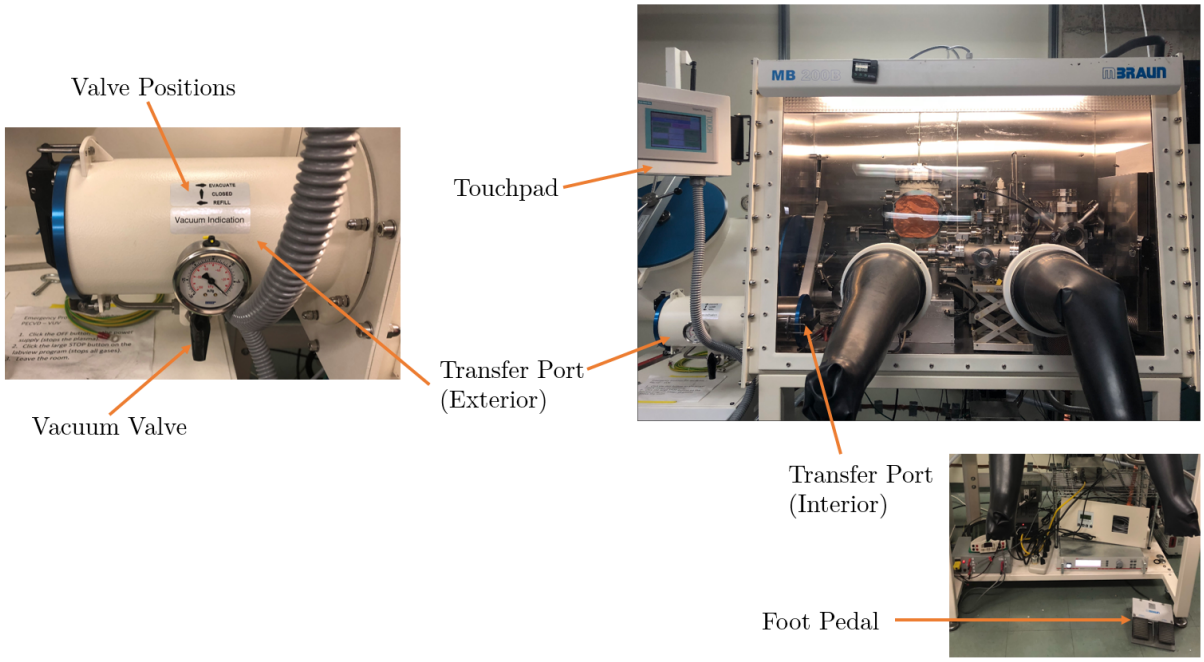

Figure A.2: The major components of the glove box are shown above.

- Argon etching is an option for XPS analysis that layer-by-layer digs into the sample surface and analyses the atomic composition. It is a suitable option when you have a lot of nanoparticles on your surface and you're more curious about the composition on the structures. It would be wise to determine the thickness of the nanoparticle layer before doing this type of analysis.
- Ensure that the X-ray spot size is suitable for the type of structures generated.
- High composition of silicon and calcium are indicative of dust and oils on your surface. Ensure that you handle your samples with gloves and tweezers; and wipe your surface clean with acetone immediately before experiments.

Appendix B: Major Equipment Data

B.1 Vacuum Pump

The vacuum pump is an Alcatel single stage rotary vane pump type 1004A, 60 Hz. The full user manual is available in the BSEL Dropbox folder in *Micromachining/Manuals/Alcatel 2004A to 2020A Users Instruction Manual*. The pump has a air displacement rate of 5.4 m^3/h. It has an inlet and exhaust NW/KF 25 flange. Page 29 of the user manual details typical issues that may arise with the pump and the remedies necessary to alleviate the problems.

The oil mist eliminator for the pump is a filter that removes oil droplets and particles from the exhaust gases; it has an orange side and a black side. The black side is connected to the pump via a NW/KF 25 flange, o-ring and clamp. During my experiments, the flange broke from the body of the oil mist eliminator. The flange was repaired with a combination of Loc-tite and gorilla glue. If the oil mist eliminator is not connected to the pump, the pump will not function correctly. Thus, pay attention that there are no leaks in the flange connection and handle the oil mist eliminator with care.

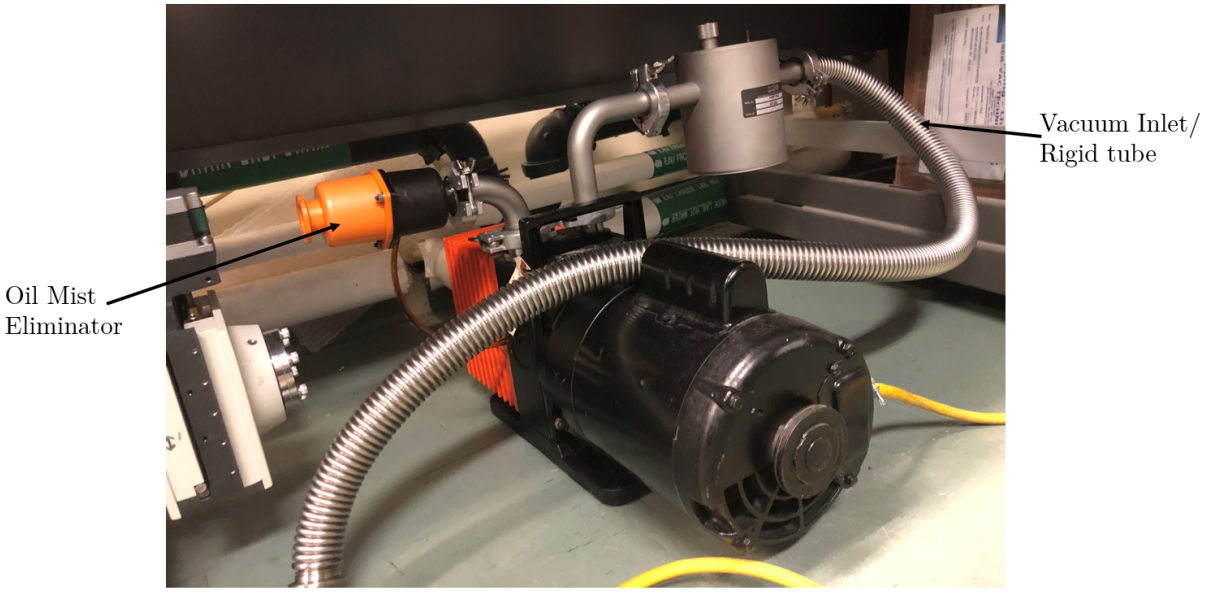

Figure B.1: An image of the vacuum pump showing the oil mist eliminator at the pump outlet and the rigid tubing leading to the pump inlet.

B.2 VTM

The Vacuum Transfer Module (VTM) is specifically designed for the K-Alpha 8/5.08. Its operating manual is located in the BSEL Dropbox folder in *Micromachining/Manuals/VTM Manual*. THe VTM consistes of three parts: the sample cover, the sample base and the retaining plate. Samples are loaded onto the base, protected with the sample cover and the retaining plate secures the cover until vacuum is established in the VTM assembly.

The sample plate can be mounted in different positions depending on the thickness of the sample (refer to page 4 of the manual). When loading into the XPS ensure that the side marked "FRONT" is at the front of the XPS apparatus load-lock. The VTM's clips will engage with the edges of the load-lock if properly fitted.

Always wear gloves when handling the VTM and only clean it with ethanol. The VTM must always be stored in its carrier case when not in use.

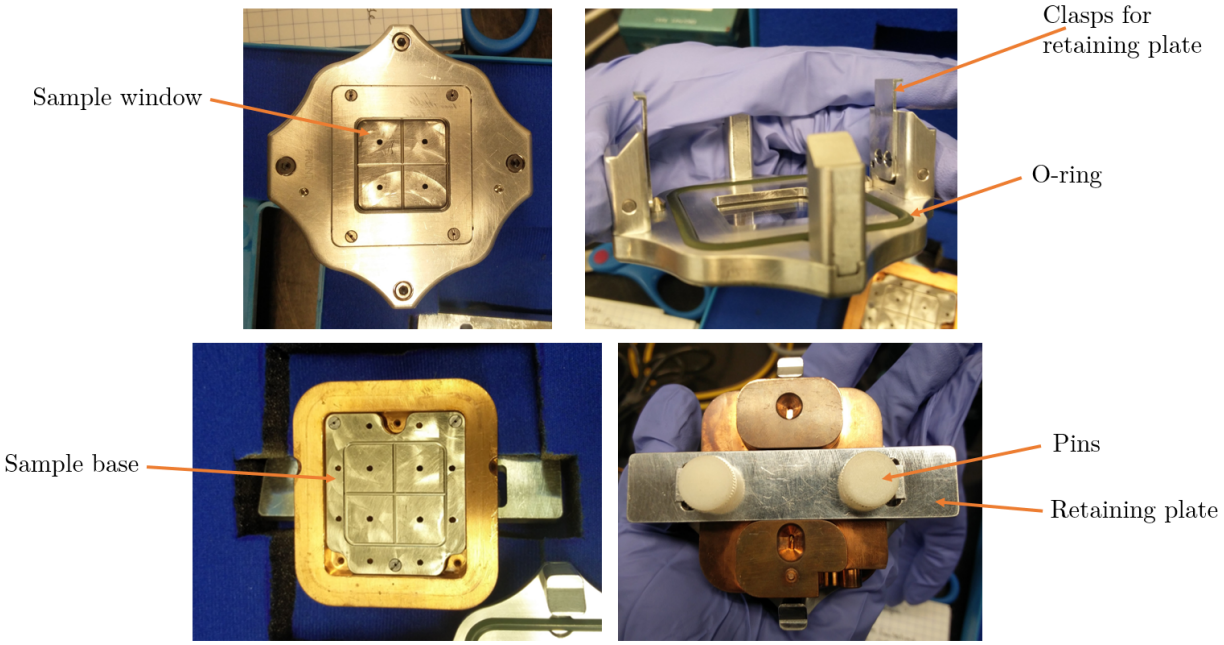

Figure B.2: An image of the VTM and its components.